JOURNAL OF GEOPHYSICAL RESEARCH, VOL. 95, NO. B5, PAGES 6829–6851, MAY 10, 1990

P and *S* Wave Travel Time Inversions for Subducting Slab Under the Island Arcs of the Northwest Pacific

HUA-WEI ZHOU [1] AND ROBERT W. CLAYTON

Seismological Laboratory, California Institute of Technology, Pasadena

We have observed slablike high *P* and *S* velocity anomalies around the Wadati-Benioff zone under island arcs of the northwest Pacific through travel time tomographic inversions. Nineteen years of International Seismological Centre travel time residuals for events and stations in this large region are used. Analyses of resolution and noise show that the images are generally well resolved. The images illustrate that slab anomalies are continuous along strike in most parts of the upper mantle of the region and become contorted and generally broadened with depth. Near the bottom of the upper mantle, fingering of the slabs, including segmenting and spreading, is indicated. The fast anomalies associated with the Japan, Izu-Bonin, and Mariana subduction zones tend to flatten to subhorizontal at depth, while downward spreading may occur under parts of the Mariana and Kurile arcs. The fast anomalies below 700 km are not in the shape of a single coherent sheet. The principal compressional axes of focal mechanisms in the region consistently follow the downdip direction of the high-velocity slab, even when it bends to subhorizontal at depth. The depth at which compression begins to dominate the downdip stress regime in the slab apparently depends on bending of the slab and its dip. Slab fingering and intense deep seismicity probably are the consequence of the slab encountering a barrier of some form around the "670-km" discontinuity.

1. INTRODUCTION

A descending lithospheric slab at convergent margins is a fundamental element in the theory of plate tectonics. Investigations of the morphology and physical state of the subducting slabs, in turn, are important for understanding plate consumption, mantle convection, origin of island arc systems, and structural discontinuities in the mantle. Numerous studies have addressed the fate of the slab and the mechanism of subduction. The seismic method is the most direct probe of the slab. Early workers [*Honda*, 1934; *Wadati*, 1935; *Gutenberg and Richter*, 1954] described the narrow slablike seismicity or deep earthquake zone, now called the Wadati-Benioff zone. Studies of earthquake focal mechanisms [*Isacks and Molnar*, 1969, 1971] revealed the stress regime of the slab to be generally extensional from the surface down to about 300 km and downdip compressional below. Due to the extinction of seismicity below about 680 km [e.g., *Stark and Frohlich*, 1985] and the possible existence of aseismic subducting slabs, observables other than seismicity are required to proceed further. Seismic travel times and amplitudes are among the most informative quantities about the morphology of slabs [e.g., *Toksöz et al.*, 1971]. It is well known that the descending oceanic lithosphere possesses anomalously high-Q and high-velocity to a depth of several hundred kilometers beneath the arc, sandwiched by two low-Q, low-velocity zones in the upper mantle [e.g., *Utsu*, 1971]. Consequently, the morphology of high-velocity anomalies, associated with subduction zones, is a good indicator of the morphology of subducted lithospheric slabs.

Seismic studies of the slab have utilized both modeling and inverse approaches. Examples of the former include the travel time residual sphere studies by *Jordan* [1977] and *Creager and Jordan* [1984, 1986]. These authors suggested penetration of the lithospheric slab into the lower mantle in the same region which is examined in the current paper. Some fast velocity anomalies found by them under the Kuriles have received support from waveform modeling [*Silver and Chan*, 1986]. There are also regional least squares type inversions in Japan [*Hirahara*, 1977; *Hirahara and Mikumo*, 1980], southwest Japan [*Hirahara*, 1981], Izu-Bonin Trench [*Roecker*, 1985], and the central Aleutians [*Spencer and Engdahl*, 1983; *Engdahl and Gubbins*, 1987]. These studies generally indicate large high-velocity anomalies at shallow depth and a decrease of the slab related seismic anomaly below about 300 km. Although these studies have yielded some important constraints, three basic questions, in our opinion, remain unanswered. They are, does the slab penetrate into the lower mantle, what is the vertical morphology of the slab, and what is the nature of the slab along its strike? In this paper we address these questions.

We use a tomographic inverse approach for a relatively large region to transform travel time residuals into a three-dimensional image of slowness (reciprocal of velocity). Any modeling approach is a "model to data" process. An inverse approach, in contrast, transforms "data to image to model." Thus the data are uniquely transformed into an image in the first stage for a given set of parameters; the image can be interpreted, though nonuniquely, in the second stage. This is analogous to reflection seismology, where data are imaged into seismic profiles and then interpreted geologically. We have used over 130,000 *P* wave travel times and over 56,000 *S* wave travel times from the International Seismological Centre (ISC) catalog for the region. The resulting images contain useful information, including constraints on the slab, as well as noise. The images, along with our interpretation of slab morphology, are presented in this paper.

The inversion method used in this study is modified from the Simultaneous Iterative Reconstruction Technique (SIRT) of *Gilbert* [1972], which is closely related to the algorithm by *Dines and Lytle* [1979]. With various modifications, this method has been used in global [*Clayton and Comer*, 1983; *Hager and Clayton*, 1989; *Zhou and Clayton*, 1985; *Davies and Clayton*, 1986] and regional [*Humphreys et al.*, 1984; *Grand*, 1987; *Humphreys and Clayton*, 1988] studies. Application of seismic tomography to subduction zones is very promising because of the distinctive velocity anomalies and the large number of deep earthquakes associated with the slabs. The abundance of earthquakes, including deep-focus ones, makes a good ray coverage for the inversion. Waves propagating from a deep source will not be triplicated by velocity discontinuities above the source; such triplications complicate inversions from shallower sources. In addition, the distribution of seismicity provides a useful check on

[1]Now at Department of Geosciences, University of Houston, Texas.

Paper number 89JB03455.
0148-0227/90/89JB-03455$05.00

the interpretation of the slab image, since it is generally accepted that deep events occur in association with the descending lithospheric slab.

Furthermore, the well-known peaks of seismicity and seismic energy release below 300 km [e.g., *Isacks et al.*, 1968; *Richter*, 1979; *Vassiliou and Hager*, 1988] are clearly present in this region, suggesting a possibly complicated morphology of the deep slab. Hence imaging of slabs in the transition zone (*i.e.*, from 400 km to about 670 km; see *Anderson and Bass* [1986]) is extremely important in understanding the mechanism and fate of subducted lithosphere.

One phenomenon that we observed is a segmentation of the deep slab into "fingers" which spread in different directions. We call this "fingering," to distinguish it from "segmenting," which has been used in subduction zone studies to describe breaks of a slab perpendicular to strike at relatively shallow depth. For instance, *Isacks and Barazangi* [1977] have investigated lateral segmentation along many subducted plates and concluded that segmentation is one of the important factors enabling more uniform bending of plate along each segment. The term fingering used here, however, emphasizes the possibly different fates of segments. As described in previous reports [*Zhou and Clayton*, 1987; *Zhou*, 1988], fingering of the slablike fast anomaly is apparent in some places near the "670-km" discontinuity.

2. Data and Corrections

All the travel time residuals used are relative to the *Jeffreys-Bullen* (JB) velocity model and are directly selected from the ISC catalog from 1964 to 1982. The raw data consists of 306,729 picks of *P* waves and 151,171 picks of *S* waves. All source locations are between 0-60°N and 115-164°E and station locations are between 10-72°N and 100-180°E (*i.e.*, the area shown in Figure 1). Except near the edge of the region each ray path is entirely, or mostly, contained in the modeled region. Inversion blocks containing less than five rays are treated as uncovered blocks during our inversions.

This region contains some of the deepest and most active

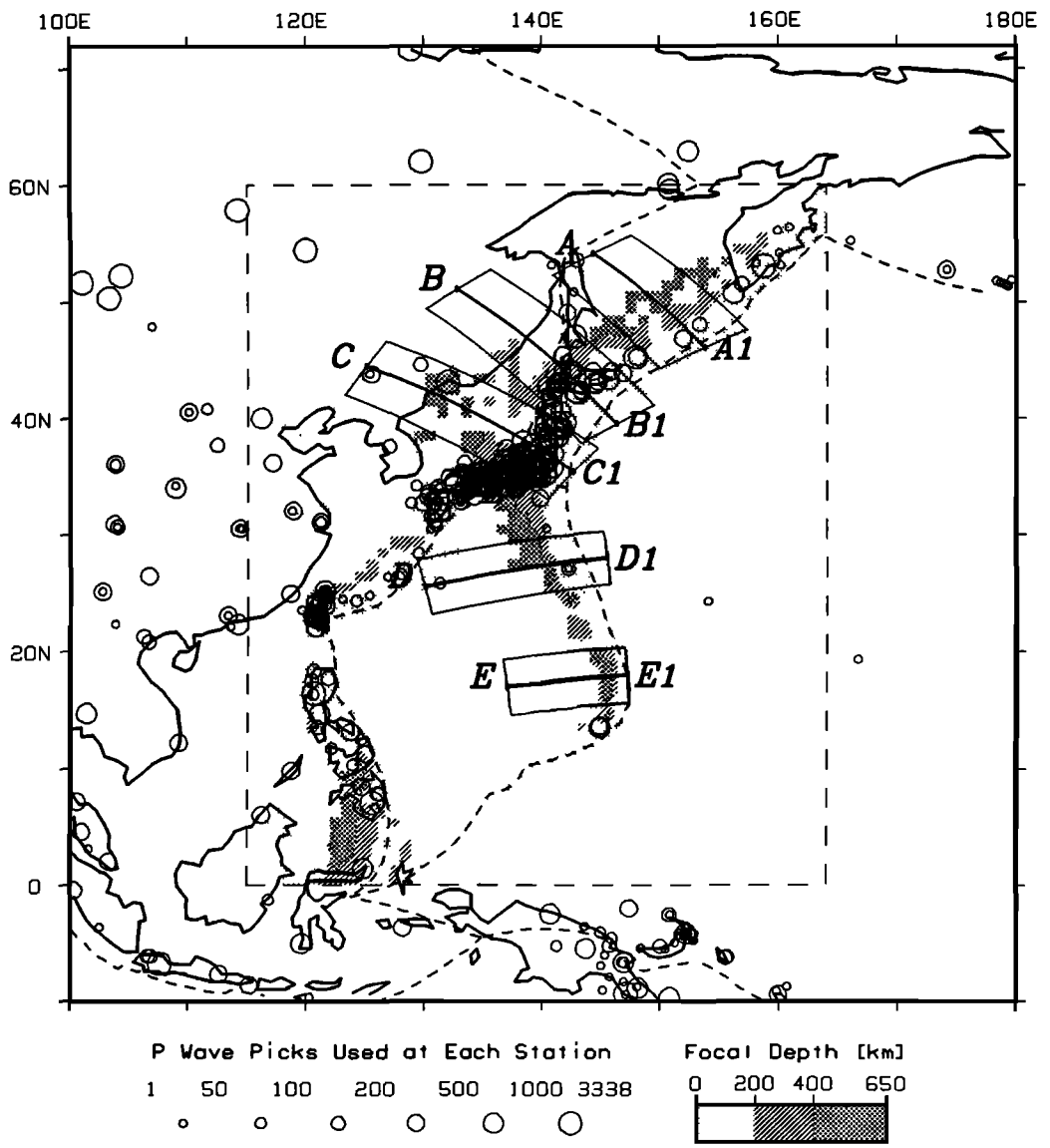

Fig. 1. Tectonic map around Island Arcs of the Northwest Pacific. The stations are circles, with their sizes indicating the number of *P* wave picks utilized. Some cocentric circles indicate either very close-by stations or a station which has been renamed. The events used are in the shaded areas inside the dashed box. Small boxes with labels "A" to "E" cover the locations of stacked vertical slices along the trench in Figure 11, and the solid lines in the middle show the locations of vertical slices in Figure 10.

subduction zones in the world, and has about one half of the global deep seismicity. The deep seismicity provides good ray coverage, and no triplications can be caused by a low-velocity zone or a velocity discontinuity shallower than the earthquakes. *Nolet* [1985] in assessing the applicability of three types of methods commonly used in seismic tomography, concluded that regions of deep seismicity may be the only places where one can hope to resolve detailed three-dimensional structure in the upper mantle. We have deep crossing rays that bottom below the deepest earthquakes. This is an optimal situation for resolving deep slab structure.

Much of our emphasis is on data reduction to improve the data quality. Our first concern is the uncertainty in source locations, because the velocity heterogeneity associated with a subduction zone can be very large. The hypocenter uncertainty of teleseismically located deep events is usually less than 20 km [e.g., *Spencer and Engdahl*, 1983]. *Barazangi and Isacks* [1979] show that for earthquakes deeper than 50 km the locations based on teleseismic data show no substantial bias or distortion of the spatial distribution. This conclusion is supported by *Nieman et al.* [1984] with theoretical computations. The ISC earthquake locations, particularly for the deep ones, are generally in good agreement with other more careful determinations [e.g., *Hirahara*, 1981; *Giardini and Woodhouse*, 1984; *Engdahl and Gubbins*, 1987; *Bock*, 1987]. In the northwest Pacific region there are stations above most of the events to obtain a good focal depth control. *Zhou and Clayton* [1988] combined source relocation into the iterative velocity inversion in the Tonga region and traced rays during the iterations. Less than 10% events there were found to have source mislocation exceed 10 km, with station coverage as good as those used for this study. The block sizes used in this study are 1°x1°x50 km and 2°x2°x50 km, much larger than average uncertainty in source locations.

One of the greatest difficulties in source relocation is that there is no a priori knowledge of the three-dimensional velocity structure. We would like, in an ideal case, to invert the system iteratively and calibrate both travel time residuals and path lengths for source locations and perturbations of ray paths by a three-dimensional ray tracer after each iteration. With a large data set, such as the one used in this study, however, it is currently impractical to adopt the above method. As a first-order attempt, we use a ray tracer based on a one-dimensional velocity model and assume that the ray paths are fixed in order to make the computation feasible. Consequently, no source relocation is involved in this study since the original ISC locations are also based on the one-dimensional JB velocity model. We attempted to select those events that are relatively well-located. First, we eliminated all events shallower than 60 km, since they usually have large location uncertainties. Second, each selected event has to be observed by more than 50 stations in the model region (the total number of stations used for source location is much greater), to insure a wide aperture for source location. Third, we iteratively removed average travel times, or statics, at stations and sources. The station statics represent near-station heterogeneities, while the removal of source statics tends to reduce the effect of mislocation. The fact that the *P* and *S* wave images from the current inversions correlate well in most parts of the upper mantle indicates that the effect of source mislocations is small, since the *S* wave data were not used in ISC hypocentral determinations.

The epicentral distance range of the data goes from nearly zero to about 75°. Stations outside the region shown in Figure 1 are not included in order to minimize parallel rays with little or no crossings. Hence this is an inversion with few teleseismic rays. In order to avoid any artifact that may be introduced by a cutoff of data over a certain distance range, we keep the picks across triplication ranges caused by velocity discontinuities in the mantle and assume that they are all first arrivals. This assumption is justified since the data are not obviously offset or more scattered in the possible ranges of the triplications.

Rays with travel time residuals greater than 10 s for *P* waves or 12 s for *S* waves are discarded initially to avoid obvious mispicks. Note that 10 s of *P* wave travel time residual corresponds to a ray that traverses more than 1400 km of 7% fast heterogeneities without encountering any slow anomalies, for a background velocity of 10 km/s. Furthermore, we excluded rays with ratios of residual over path length greater than 12% of the reference slowness at their source. This exclusion is designed to avoid erratic readings at short distances. A correction for Earth ellipticity is also done following *Dziewonski and Gilbert* [1976].

We then grouped rays into the same source and station areas and eliminated those residuals which deviated significantly from the residual median (which better approximates the trend of the data than the average) of each group. Of course, decisions about the size of the source and station areas and the maximum deviation are quite subjective. Small areas and cutoff values lead to better data quality but poorer ray coverage, a typical trade-off between error and resolution. We tried a series of different area sizes and cutoff values to find optimal values that minimize ray elimination. The area size finally used was 1°x1°x25 km for both *P* waves and *S* waves. The maximum deviations taken for *P* waves are 1.2, 1.6, and 2.0 s for groups of two rays, three rays, and more than three rays, respectively. The corresponding maximum deviations for *S* waves are 2.5, 3.2, and 4.0 s. All one-ray groups are eliminated. This "grouping and sorting" process greatly reduces the high-frequency noise (see Figure 4), but it cuts off approximately one third of the data. As discussed later, in section 4, this process improves the internal consistency of the data. We consider that this kind of sorting is important and necessary to reduce the inconsistent noise which is definitely present in ISC data.

3. ITERATIVE INVERSION

An iterative inversion scheme by R. P. Comer and R. W. Clayton (unpublished manuscript, 1984) is used in this study with a large number of model blocks of constant velocity perturbations. We have *M* observed travel time residuals given by a vector Δt and slowness perturbations for each of *N* blocks parameterizing the region given by another vector Δs. Assuming that a spherically symmetric reference velocity model, such as the JB model, is adequate for the region, we are then able to linearize the travel time problem in the form of

$$\Delta t = L\Delta s \tag{1}$$

where L is a $M \times N$ matrix which contains the path length segment of each ray in each block. Our goal is to invert slowness perturbations Δs from known residuals Δt and path length matrix L. L is determined from tracing rays in the block grid.

The recursive formula from the *(n-1)*th iteration to the *n*th is, following the SIRT back projection scheme by R. P. Comer and R. W. Clayton (unpublished manuscript, 1984)

$$\Delta s^{(n)} = \Delta s^{(n-1)} + SL^T DL\left[\Delta t - \Delta t^{(n-1)}\right] \tag{2}$$

where I is an unit matrix, $S = \mathrm{diag}\left(1/(\mu + L_i^M)\right)$ and $D = \mathrm{diag}\left(1/L_k^N\right)$. Here μ is a damping factor,

$$L_i^M = \sum_{j=1}^{M} l_{ji}$$

is the sum of all path lengths through the *i*th block, and

$$L_k^N = \sum_{j=1}^{N} l_{kj}$$

is the entire path length of the *k*th ray.

We adopt a method by *Olson* [1987] to accelerate the convergence by modifying S to

$$S = \frac{2}{1+\alpha\sigma^{(n)}} \operatorname{diag}\left(\frac{1}{L_i^M}\right)_{N\times N} \quad (3)$$

where the 1 in the denominator is necessary to keep the inversion stable, because all singular values of $\mathbf{D}^{1/2}\mathbf{L}\mathbf{S}^{1/2}$ need to be less than $\sqrt{2}$, according to R. P. Comer and R. W. Clayton (unpublished manuscript, 1984). On the other hand, α is a positive weight for $\sigma^{(n)}$, the zeroth root of the Chebyshev polynomial for nth iteration as described by *Olson* [1987]. We set α to 1.0 in this study. One can regard the product $\alpha\sigma^{(n)}$ as a variable damping factor; $\sigma^{(n)}$ is unity during the first iteration of inversion and decreases monotonically during the following iterations to accelerate the convergence.

As mentioned earlier, we assume all the ray paths to be fixed in our computation. Since we do not know a priori the proper block size, we have performed inversions on two grids of different block sizes. The block size of the first grid is 2° laterally and 50 km in depth, while the block size of the second grid is 1° laterally and 50 km in depth. These two different grids resulted in very similar velocity models (see Figures 7 and 8).

4. Resolution and Noise Estimation

Estimations of the resolution and noise are extremely important for interpretation of the inverse images. For the scheme of tomographic inversion used in this study the conventional resolution matrix at the nth iteration are related to the resolution matrix at the first iteration by

$$\mathbf{I} - \mathbf{R}^{(n)} = (\mathbf{I} - \mathbf{R}^{(1)})^n \quad (4)$$

where $\mathbf{R}^{(1)} = \mathbf{S}\mathbf{L}^T\mathbf{D}\mathbf{L}$. Hence $\mathbf{R}^{(n)}$, the mapping matrix from the true model to the resolved model at the nth iteration, depends entirely on the data ray paths. Since the dimension of the model space N is usually very large, it is impractical to use equation (4) to compute the resolution matrix directly.

In this study, we evaluate the resolution with an approximation which is based on the following synthetic test. A synthetic model is constructed with a slowness perturbation at the location of interest, such as in the subduction zone. The real data paths are used but the travel time residual for each ray is computed by ray tracing through the synthetic model. Two examples of comparison between given models and the corresponding solutions are shown in Figure 2. In the first case (Figure 2*a*), the high-velocity model has a low dip angle, which is usually difficult to resolve with teleseismic rays alone. Our generally satisfactory resolution is due to the use of regional picks ($\Delta < 25°$) and deep earthquakes. The model in the second case (Figure 2*b*) is under the central Izu-Bonin trench where seismicity becomes flat around 550 km depth. This model has a rather unusual shape, combining a vertical high-velocity column (not a slab) which bends slightly in the middle and a vertical column which bends in the middle. The inversion has properly recovered the shape of the model but underestimated the amplitude in some places, particularly in the lower mantle.

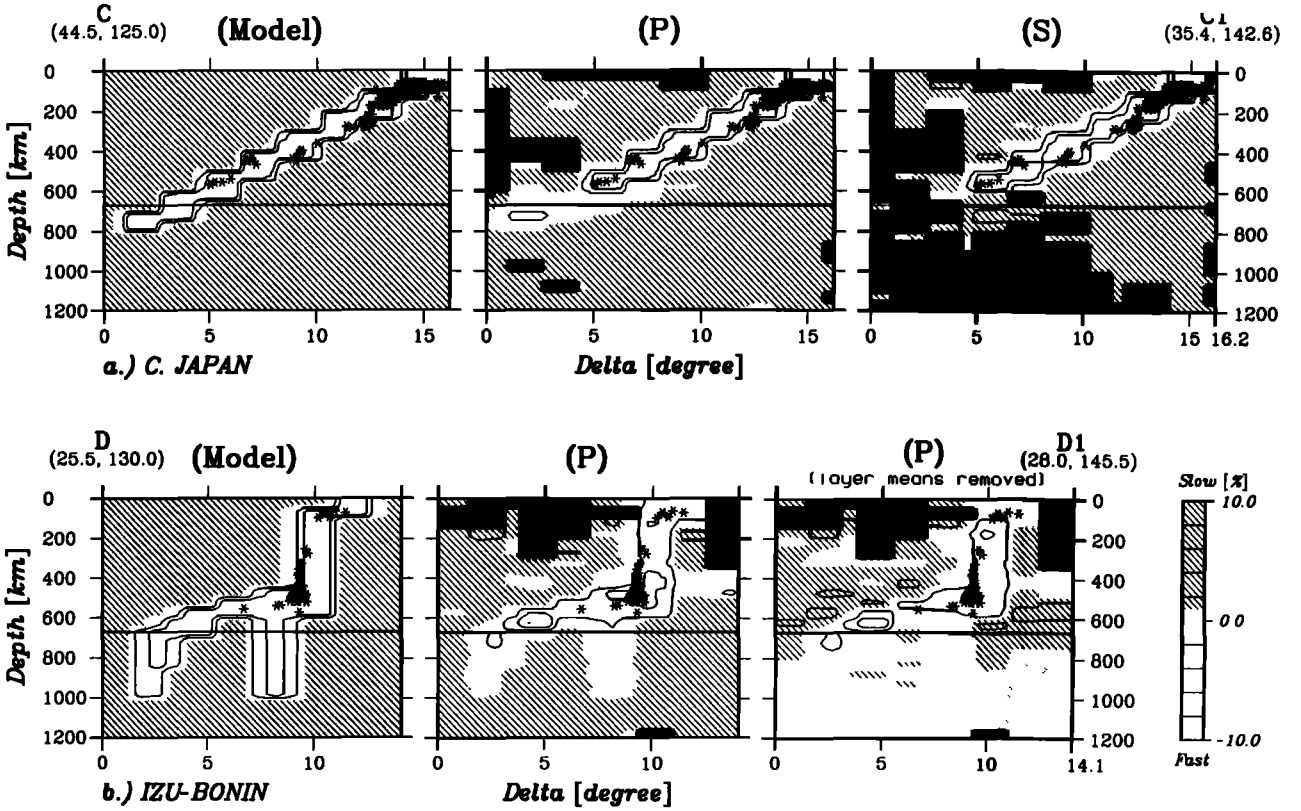

Fig. 2. Comparison of synthetic models with corresponding solutions. The left panels in Figures 2*a* and 2*b* are the synthetic models. The middle and right panels in Figure 2*a* are the *P* and *S* wave solutions, respectively. Both the middle and right panels in Figure 2*b* are the *P* wave solution, and the right one has the mean layer velocities removed. The stars denote earthquake foci. The slowness perturbations are contoured with an interval of 2%. The solid areas are blocks with less than five passing rays, defined as uncovered. In the covered areas, the open areas are fast, cross-hatched areas are slow, and dotted areas are of less than one half of the contour interval, or 1.0%, of slowness perturbations. The patterns of the models are recovered well by the inversions, while the amplitudes are underestimated in some places.

Generally, the resolution for pattern is good, but the resolution for amplitude is poor, particularly at depth. Notice that the removal of layer mean velocities in the right panel of Figure 2*b* enhances the coherency of the pattern. This kind of enhancement was used for real data images because we are mainly interested in relative velocities.

The idea behind the above test leads to our approximation, called an "impulse test." To impulse test the resolution for a particular block, we first construct a synthetic model with unity slowness perturbation at the block and null elsewhere. Subsequent inversion using data ray paths and residual times generated from the synthetic model results in the column vector which corresponds to the block in the resolution matrix $\mathbf{R}^{(n)}$. The conventional resolution vector for a block is the row vector in $\mathbf{R}^{(n)}$. When $\mathbf{R}^{(n)}$ is symmetric (*i.e.*, when S in equation (3) is symmetric in the current case), the solution column vector is the true resolution vector for the block. Even when $\mathbf{R}^{(n)}$ is asymmetric, the diagonal element of the resolution matrix can always be obtained, which can partially indicate the resolution level.

The impulse test is useful to detect image smearing. The smearing will generally take place where most rays traverse the model in almost the same direction, and it will appear in the impulse test result at these locations. The impulse test is also

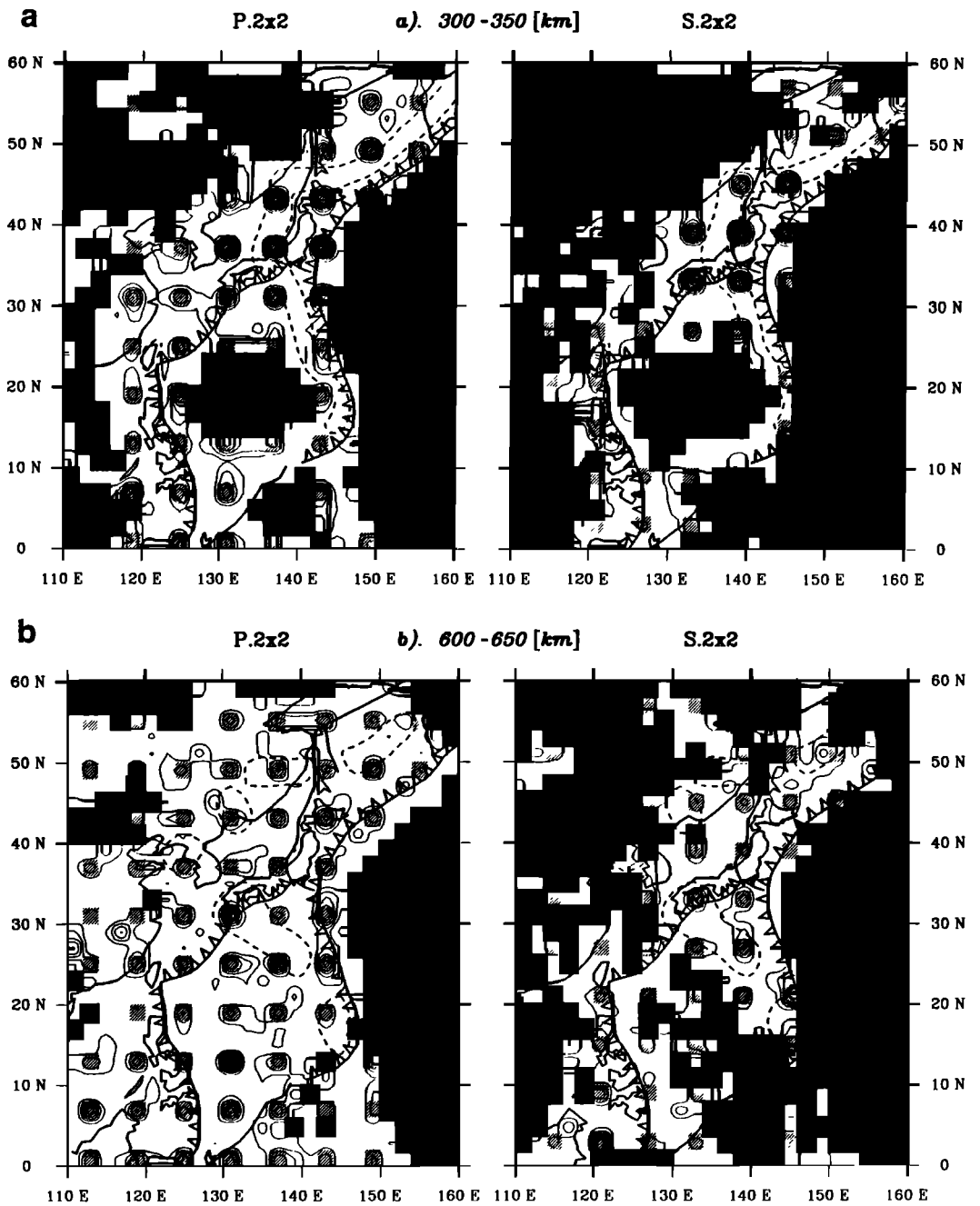

Fig. 3. Examples of resolution impulse tests. These are map views of some "impulse tests" for *P* and *S* waves at depth 300-350 km and 600-650 km on the 2°x2°x50 km grid. Cross-hatched boxes are the impulsed blocks, solid areas are uncovered, and contour interval is 0.1. The approximated location of the slab is enclosed by the heavy dashed lines. Each panel is the sum of the column vectors of the resolution matrix for the impulsed blocks. Notice that the pattern associated with each impulsed block is usually concentrated at the block, even though the amplitude is low in many cases.

used to check the amplitude of the image. In addition, when the model space is large and the resolution is expected to be sharp, one can perform many impulse tests simultaneously for many well separated blocks. In this way, we have conducted impulse tests for all model blocks in this study. As examples, horizontal slices of some impulse tests are shown in Figure 3. Notice that the contour lines are generally concentrated over the test block, even when the amplitude is very low, which happens in some cases. Poor resolution usually exists near the edge of the covered area. In general, the resolution of both compressional and shear velocities is quite sharp in most areas of interest. In particular, the resolution for pattern is uniformly satisfactory across the 670-km discontinuity, but the resolution for amplitude decreases in the lower mantle (see resolution vertical panels of Figure 10).

The noise in an image comes from the data noise and the propagation of numerical noise through the inversion. Recently, *Davies et al.* [1988] proposed that by grouping rays, e.g., groups of same source and station areas, the average group variance for very small grouping areas approximates the variance of the random noise, while the average variance for large grouping areas represents the total data variance. Following this, the effect of each data processing step, including correction, sorting, and inversion, on the data at different wavelengths can be displayed by the relation between the block size (the diagonal length in a block) and the average group variance. As shown in Figure 4 for the *S* waves (a similar plot for the *P* waves is given by *Zhou* [1988]),

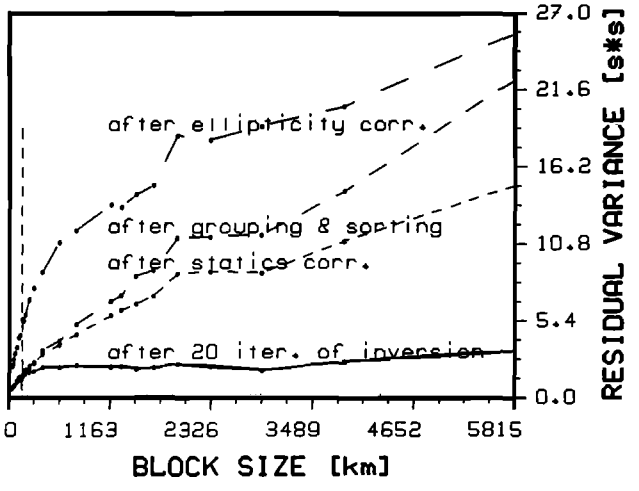

Fig. 4. Relation between the average group variance and the grouping block size (the diagonal length). The group variance is for a group of residuals of rays with same source and station areas. The curves are for the *S* wave data at different stages. The vertical dashed line at the left indicates the inverse block size of the 1°x1°x50 km, and the shaded zone at the bottom represents the noise level in the data just before inversion. Notice that the grouping and sorting procedure considerably reduces the noise level and the inversion has absorbed a large portion of the long-wavelength variations of travel time residuals.

the efficiency of each correction or sorting is judged by the reduction of the average variances at small block sizes. For example, grouping and sorting considerably improves the data quality because the sorting reduces the high-frequency noise of the data and has little effect on the long-wavelength variations. On the other hand, the static terms and the inverted image contain much of the long-wavelength variations. These are usually the informative parts of the data relating to mantle heterogeneities.

If the inversion is perfect, the residual variance curve after inversion is expected to be along the top of the shaded zone in Figure 4, the variance level at the inversion block size just before the inversion. Actually, the curve after inversion shows slight aliasing of some high-frequency noise into the image, although most of the long-wavelength variations have been absorbed by the inversion. The change of the average group variance, at a given block size during the inversion, denoted by ΔV, represents the portion of the travel time residuals that is transformed into the image at the corresponding wavelength. As a result, the random noise level in the image can be estimated as

$$(\text{Random Noise Level})_{\text{image}} = (\Delta V \text{ at the Inverse Block Size} / \Delta V \text{ at the Largest Block Size})^{1/2} \quad (5)$$

According to equation (5), the estimations of random noise levels are 25% and 17% for *P* and *S* wave models, respectively, at 2°x2°x50 km grid, and 20% and 11% for *P* and *S* wave models, respectively, at 1°x1°x50 km grid.

Furthermore, we computed the model covariance matrix in the same way as *Davies and Clayton* [1987] to evaluate noise propagation. A large number of inversions are performed using data ray paths. The travel time residuals used, however, are randomly selected from a residual distribution which is identical to the data distribution. The slowness variance for each block is then obtained from the results of all inversions. If we introduce the noise variance obtained from equation (5) into computations of the model covariance matrix, the resulting slowness variances, which are produced by random noise, are below most long-wavelength anomalies, such as the slablike fast features, in the images of the real data. Figure 5 shows features of the *P* wave structure in the 2°x2°x50 km grid that stand above the noise level as estimated above. This suggests that most anomalies in our images are reliable since they are from the long-wavelength or systematic, portion of the data.

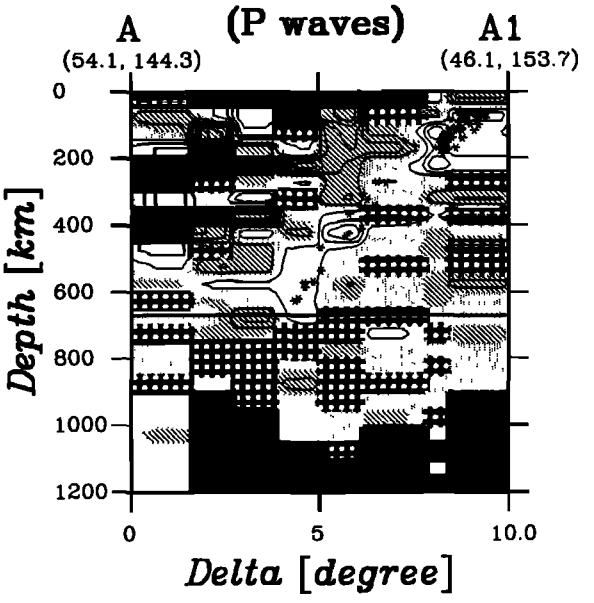

Fig. 5. The vertical slice, identical to that shown in Figure 10*a*, is of the *P* wave image under the Kurile arc. The plotting convention follows that used in Figure 2, and the contour interval is now 1%. Solid areas with little open diamonds denote blocks whose image amplitudes are below the noise level, estimated by the model covariance matrix using the noise variance estimated from equation (5).

5. RESULTS

Figure 6 shows the maps of station statics of *P* and *S* waves. Notice that features in the two maps are quite similar and

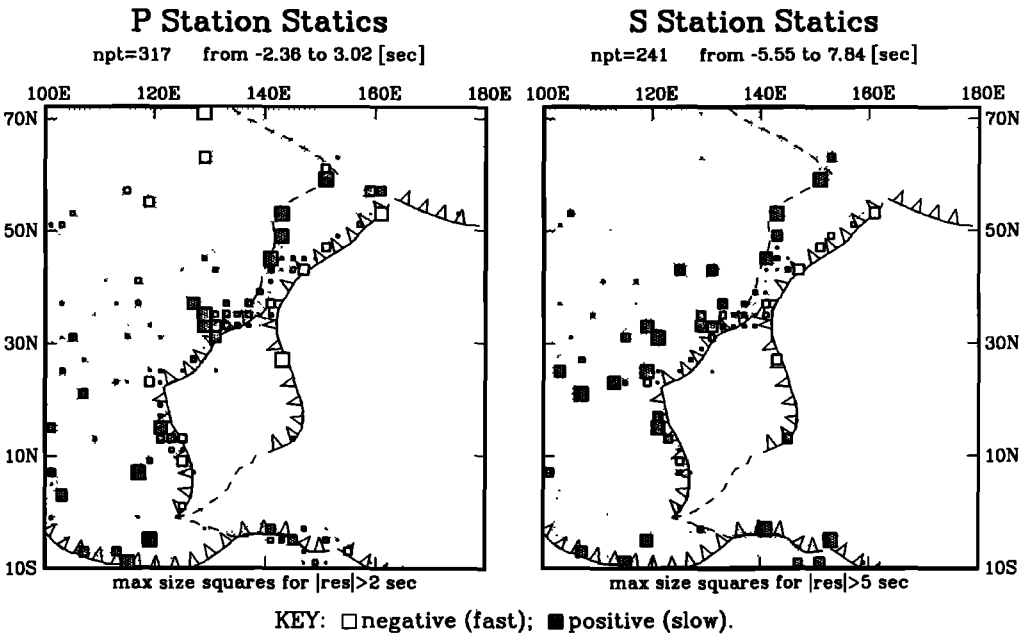

Fig. 6. Station statics. These are observed average seismic travel times at stations. The pattern of *P* waves (left panel) is generally similar to that of the *S* waves (right panel).

generally correspond well to surface tectonic patterns. The statics are fast along the Kurile, Japan, and Izu-Bonin arcs and are slow around the back arc region. For continental East Asia, *P* waves are fast, while *S* waves are slow. China is slower than the Siberian Shield. The amplitudes of *S* wave statics are about double the P wave statics. On the other hand, maps of event statics are meaningful only when they are plotted at each depth range, to account for their vertical distribution.

We define the data variance reduction as

$$\sum_{j=1}^{M} (t_j - p_j)^2 / \sum_{j=1}^{M} (t_j)^2$$

where t_j and p_j denote data and model prediction of travel time residuals, respectively, for the jth ray. The data variance reductions, in the final inversion stage alone, are 58% and 59% for *P* and *S* waves, respectively, at 2°x2°x50 km grid and 48% and 51% for *P* and *S* waves, respectively, at 1°x1°x50 km grid. A smaller block size is expected to result in a higher variance reduction, because it means more model parameters. Of course, the values of variance reduction here merely show the apparent fitting level of the inverted models. The efficiency of the inversion, however, is obscured from those values, because the presence of random noise has set an upper limit for any inversion technique. For this reason the group variance versus area size graph shown in Figure 4 is a much better illustration of the efficiency of the inversions. A comparison of the variance curves in Figure 4 before and after the inversions indicates that the inverted models in this study have absorbed most of the long-wavelength and systematic components of the data.

Before going into the results and interpretation, we would like to remind the reader that the images presented here contain noise as well as artifacts in areas of poor resolution. The effort in the last section was particularly devoted to estimating the resolution and noise levels of the images. In addition, features of dimension equal to or smaller than the block size are obviously unresolvable. Consequently, large and coherent anomalies in the images are more reliable. Seismicity distribution and principal stress directions, as inferred from mantle earthquake mechanisms, are also helpful in interpreting the high-velocity slabs associated with subduction zones. Most of the results in this section include the above considerations.

Figures 7 and 8 show horizontal slices (map view) of the *P* and *S* velocity images. The images for the two grids are reasonably similar. There are fast compressional and shear wave anomalies in the images associated with the descending lithosphere inferred from seismicity. Slab anomalies are generally continuous along strike in most parts of the upper mantle, and are often sandwiched by large amplitude slow anomalies on the arc and trench sides in the top several hundred kilometer depth range. *P* and *S* velocities correlate well over most of the upper mantle, but are less similar in the lower mantle, probably at least partially due to a decrease of resolution with depth. *Anderson* [1987*b*] pointed out that at relative low pressure and high temperature, shear velocity anomalies are expected to be similar to compressional velocity anomalies, since the temperature effect on both the bulk modulus and rigidity is very volume dependent. At high pressure, variations of seismic velocities are smaller and due primarily to changes in the rigidity.

Estimates of the average velocity variations of slabs and of ambient mantle in the upper mantle, where the resolution for amplitude is reasonably good, are listed in Table 1. These values are with respect to the average velocity of each layer. The "ambient mantle" here is taken as the region outside of the most

TABLE 1. Estimated Average Amplitudes of Slab Related Anomalies With Respect to the Average Layer Velocities

Depth, km	*P* waves, %		*S* waves, %	
	Slab	Ambient Mantle	Slab	Ambient Mantle
0-100	-4.0 to -2.0	+2.0 to +3.5	-4.0 to -1.0	+2.0 to +4.0
100-200	-3.0 to -2.0	+2.0 to +3.0	-5.0 to -3.0	+1.0 to +4.0
200-300	-3.0 to -1.0	+1.5 to +2.5	-4.0 to -1.0	+1.5 to +3.0
300-400	-4.0 to -0.5	+1.0 to +2.0	-3.0 to -2.0	+2.0 to +3.0
400-500	-3.0 to -1.5	+1.5 to +2.5	-4.0 to -2.0	+1.5 to +2.5
500-600	-2.0 to -1.0	+1.0 to +2.0	-2.0 to -0.5	+1.0 to +1.5
600-700	-2.0 to -0.5	+0.5 to +1.5	-2.0 to -0.5	+1.0 to +1.5

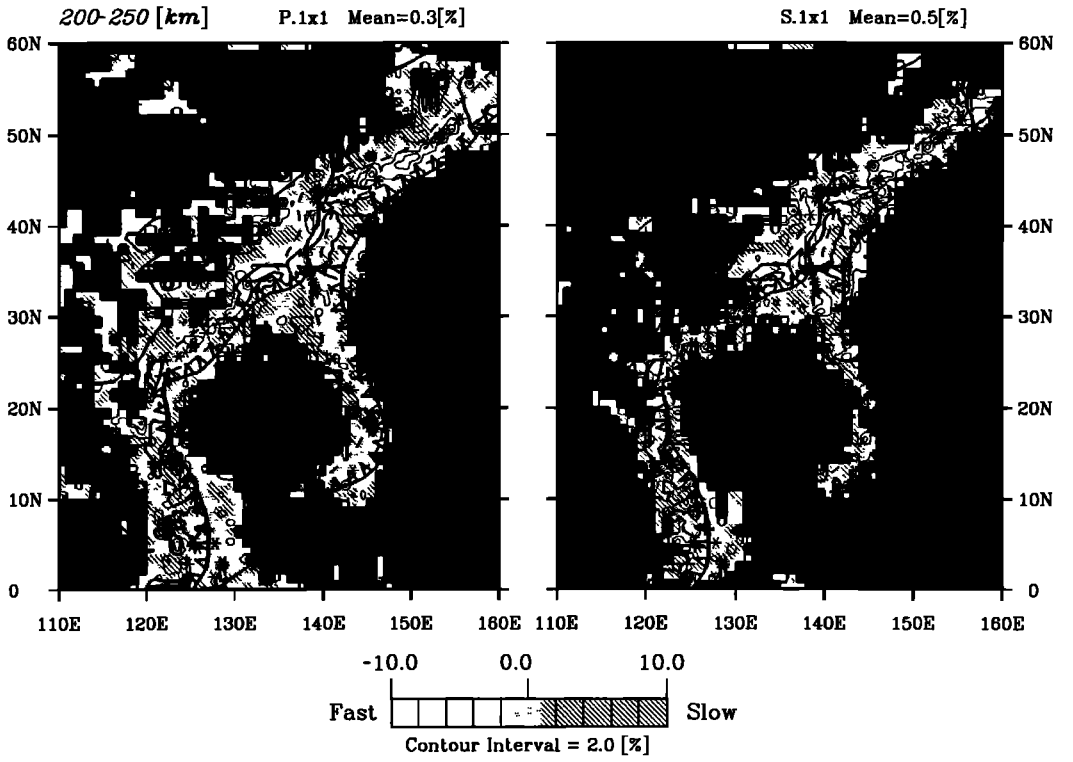

Fig. 7. Horizontal slices of the images on 1°x1°x50 km grid. The *P* (left) and *S* (right) slices shown are at depth 200-250 km. The legend convention is the same as that used in Figure 2. The trenches above subduction zones are shown with triangular teeth. The mean velocity variation of each layer, given at the top, has been removed. Our interpreted fast slab model at this depth range is indicated in heavy dashed lines, while the entire interpretation down to 800 km depth is pictured in Figure 9. General patterns in the *P* and *S* wave images correlate well. The fast slablike anomalies associated with the subduction zone and slow anomalies on both sides of slabs are shown.

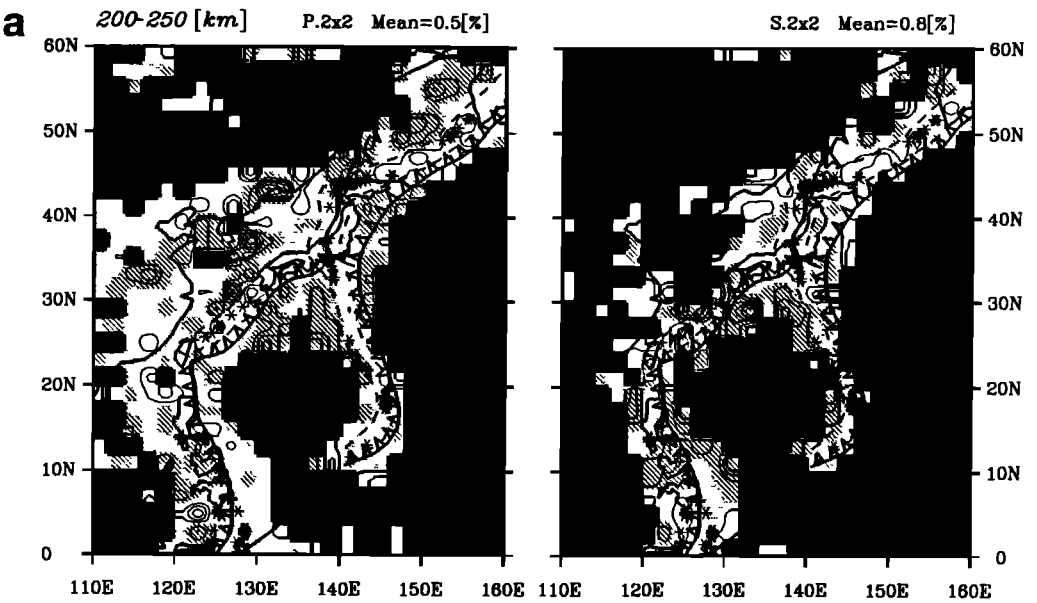

Fig. 8. Horizontal slices of the images on 2°x2°x50 km grid. Each pair in this figure shows *P* (left) and *S* (right) images at a layer of 50 km thickness. The plotting convention is identical to that used in Figure 7. Notice that the patterns in the first pair, depth 200-250 km, correlate well to the patterns in Figure 7 of the 1°x1°x50 km grid. The anomalous features, especially these which are associated with subduction zones, are somewhat correlated between adjacent panels above 650 km. However, the correlation between adjacent panels becomes much poor below a depth around 650-700 km, even though the resolution for patterns is more or less uniform across this depth.

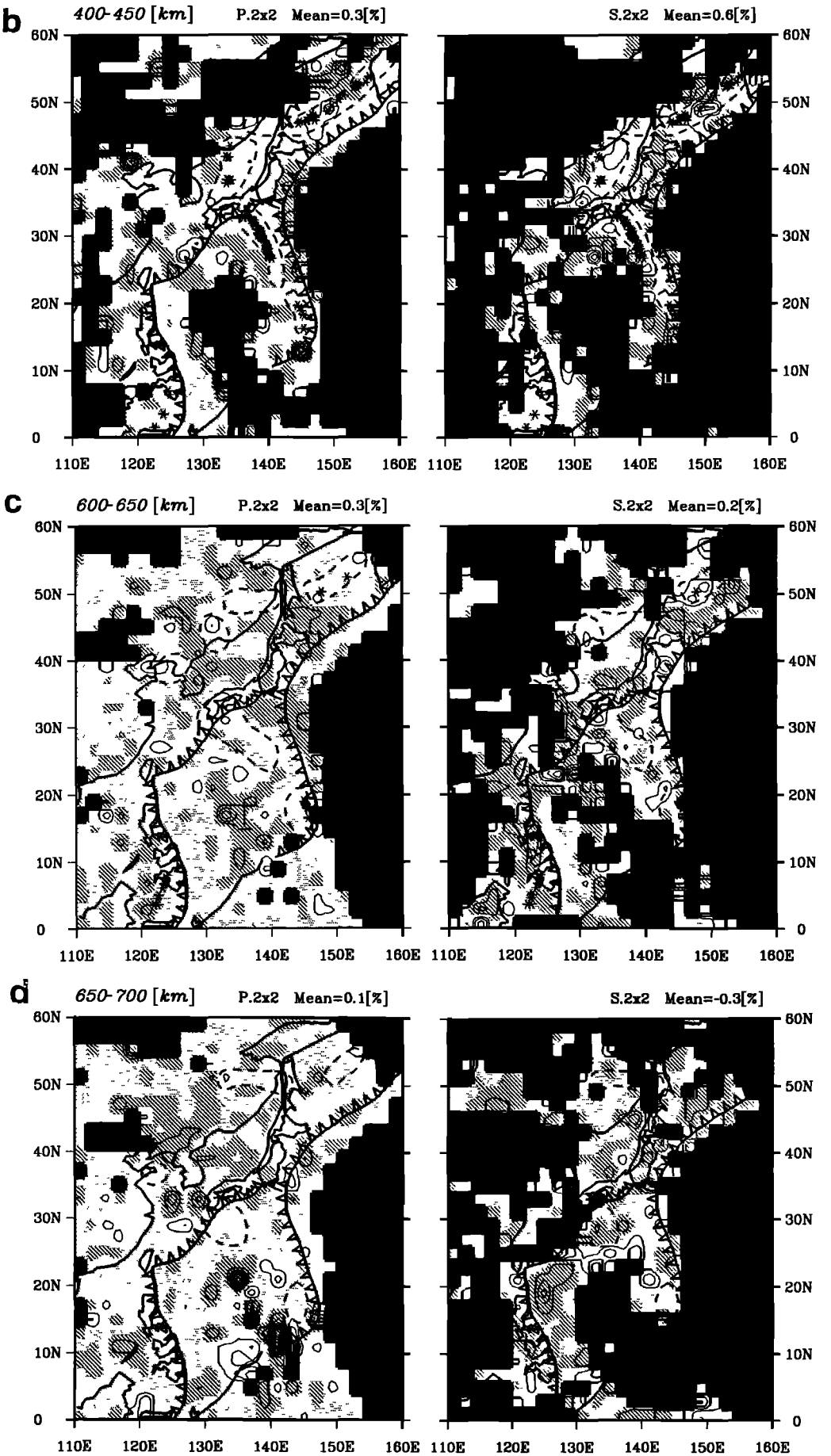

Fig. 8 (continued)

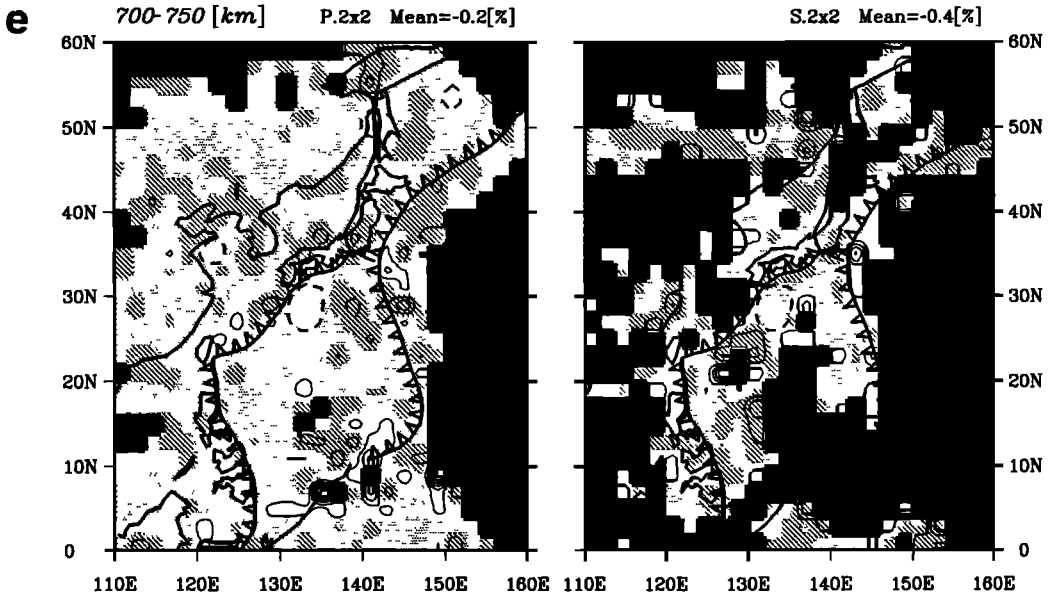

coherent fast anomalies that are associated with the Wadati-Benioff zones (the locus of the intermediate- and deep-focus earthquakes). Therefore the estimates for the ambient mantle, particular for the top 300-400 km range, are possibly slower (more positive) than the real mantle average velocity, since those regions are heavily influenced by slow heterogeneities beneath the back arc basins. The velocity contrast between slabs and their surrounding slow regions shows a large variation but reaches as high as 7-8% in the shallow mantle. The relative amplitude of the shear wave anomalies, in a laterally average sense, is about one and a half times the amplitude of the compressional wave anomalies in percentage (*i.e.*, $d \ln V_S \approx 1.5\, d \ln V_P$). The ratio is slightly lower than values estimated by some previous investigators, as described by *Anderson* [1987*b*]. The larger shear velocity variations shows that lateral variations in rigidity are more important to seismic velocity than lateral variations in bulk modulus.

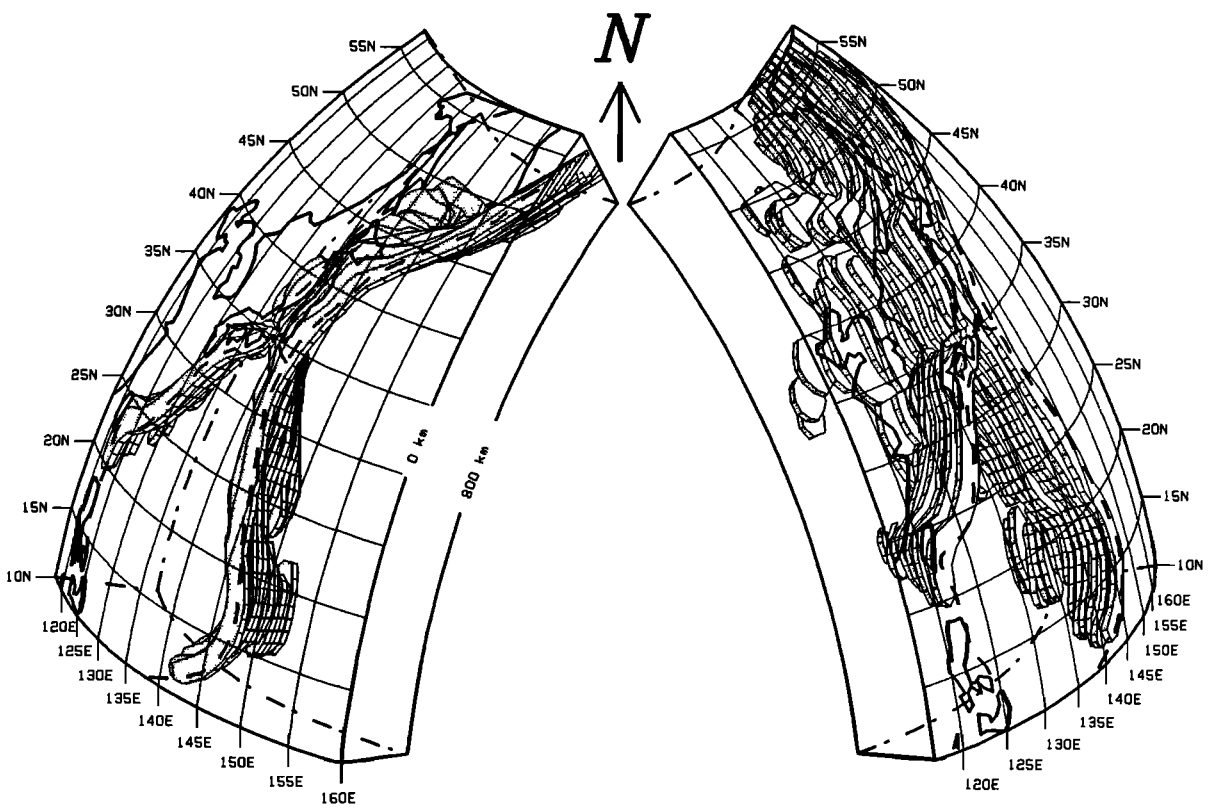

Fig. 9. Interpreted model of slab anomalies. This figure illustrates two three-dimensional views of our interpretation model of the fast velocity anomalies associated with subducted lithosphere in the region, from surface down to 800 km depth. The model is interpreted based on correlated fast features in the *P* and *S* solutions in two different block grids, layer to layer comparison, and seismicity. The model indicates the continuity of the fast slab in the upper portion of the upper mantle and the complication of fingering and spreading of the slab in the transition region.

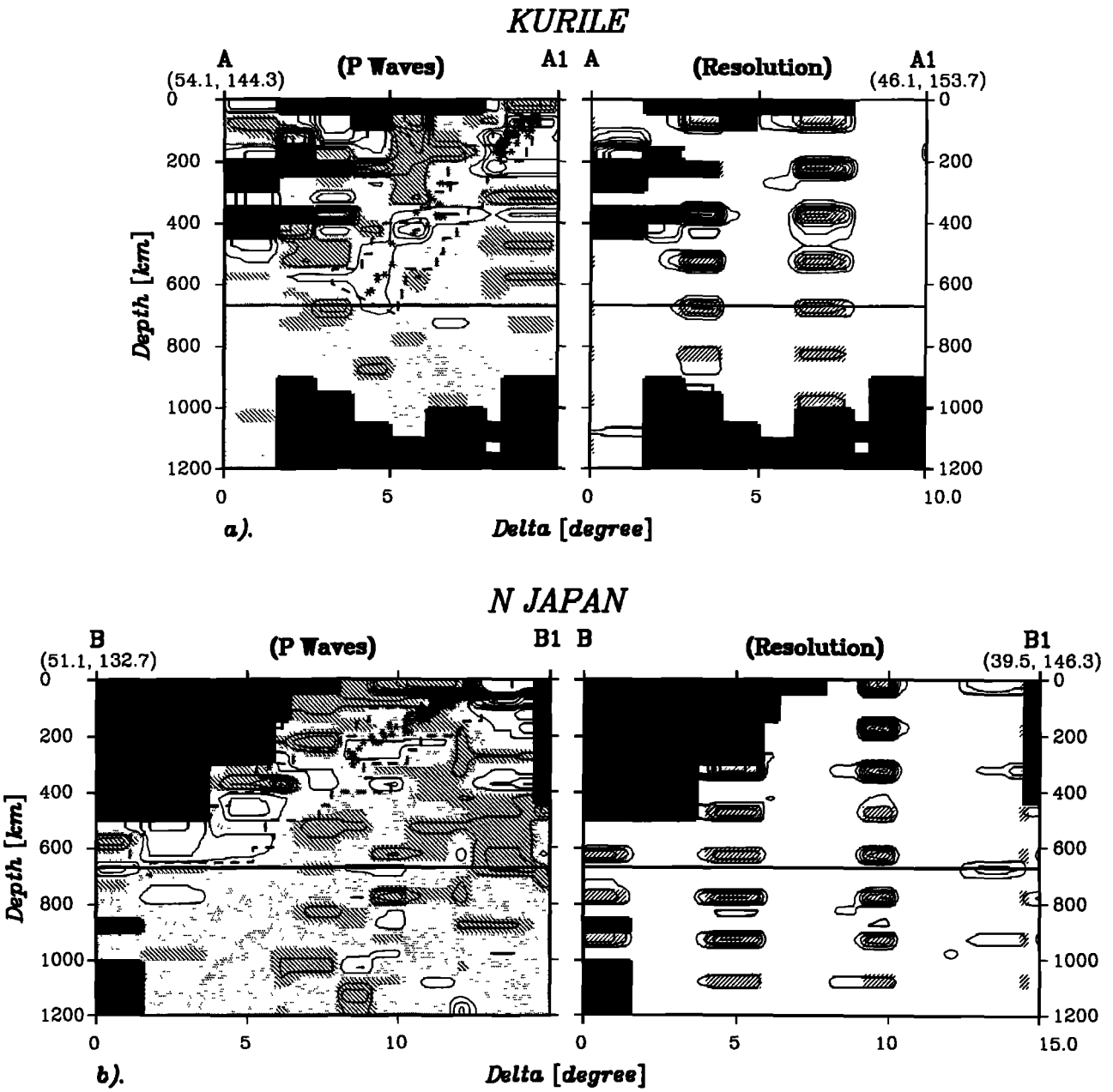

Fig. 10. Vertical slices on 2°x2°x50 km grid. The surface locations of these slices are shown as the heavy solid curves in Figure 1. Each slice is paired with the result of some "impulse" resolution tests to the right. The plotting convention for the slowness follows that used in Figure 2, except the contour interval is 1% now. The heavy dashed lines indicate the cross section of the interpreted model (Figure 9), which is a interpretation of large, coherent, and subduction-zone-related fast anomalies in the horizontal slices of the images. The depth of 670 km is indicated with a line. The plotting convention for the "impulse" tests follows that used in Figure 3. The curvature of the Earth is bent to flat, and there is approximately no vertical exaggeration. In all slices the fast slab anomalies around the Wadati-Benioff zone are clearly shown; they all broaden with depth and probably reach to the bottom of the upper mantle. The resolution is generally sharp, except in some areas under the Kurile and Mariana arcs. (*a*) Kurile, (*b*) north Japan, (*c*) central Japan, (*d*) Izu-Bonin, and (*e*) Mariana.

A three-dimensional seismic slab model for the Northwest Pacific subduction zones (Figure 9) is interpreted from horizontal slices (map views) of the *P* and *S* wave images. Anomalies in horizontal slices are usually much more stable than that in vertical slices (profiles), probably due to (1) layered images being more uniform in resolution and (2) curving and segmentation of the slab along its strike making patterns in vertical slices unstable. The interpretation is based on correlated fast features in the *P* and *S* solutions in two different block grids, layer to layer comparison, and seismicity distribution. The interpretation assumes that the fast slab model is continuous in the downdip direction in all places. Hence, in some vertical slices (e.g., Figure 10) the model is always continuous while fast anomalies along subduction zones are truncated by slow patches in some places. It is obvious that this slab model is merely one version of interpretation for the tomographic images. Even though it is arguable as how to interpret these noise-bearing images, our intention is illustrating the images with their resolution and noise aspects as well as showing "our version" of slab interpretation.

The model covers the seismic slabs under the Kurile, Japan,

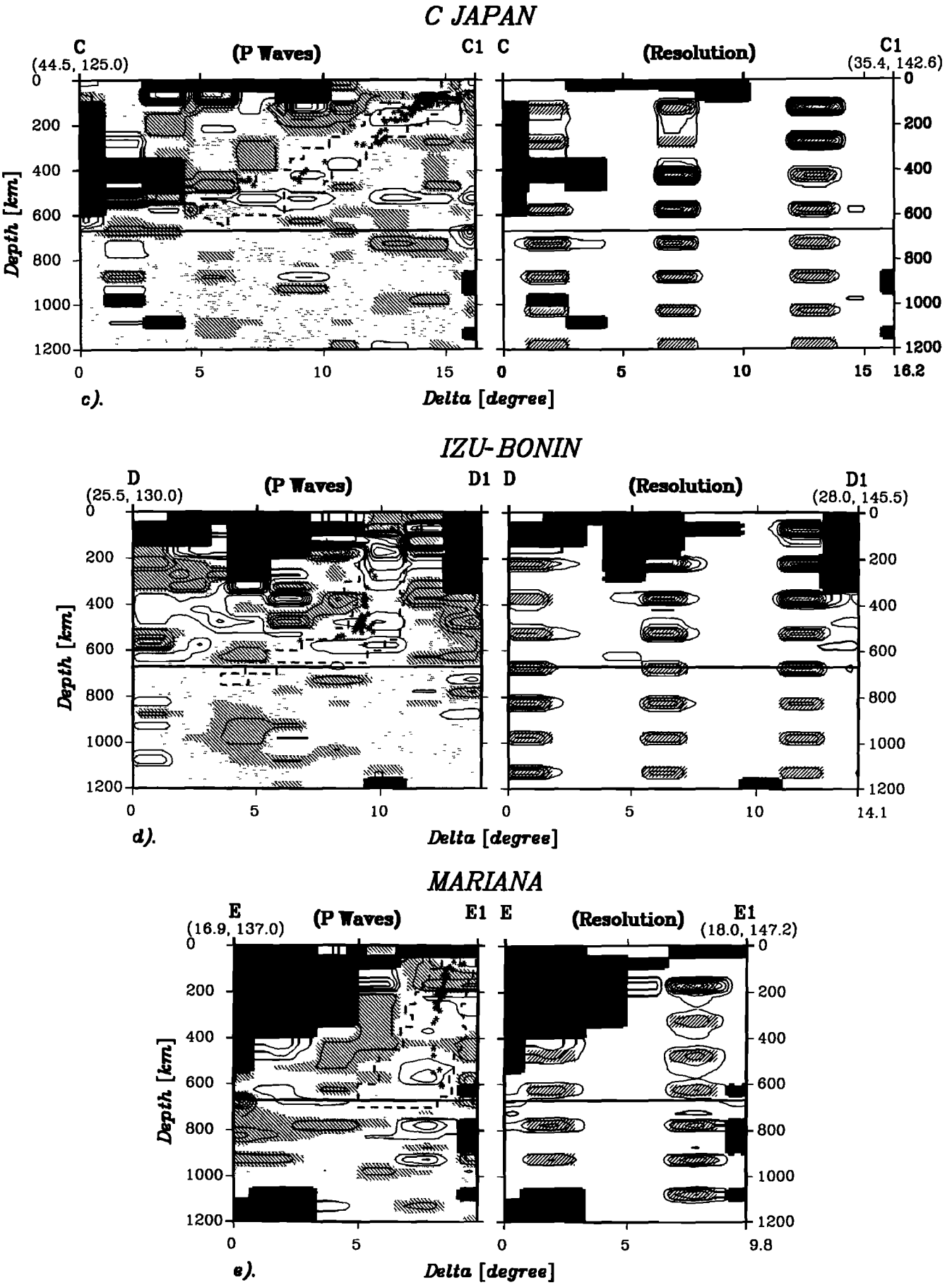

Fig. 10 (continued)

Izu-Bonin, Mariana, and Ryukyu arcs, from the surface down to 800 km depth. No interpretation is given for the Phillippine arc since data coverage is not adequate there. We terminated the interpretation at 800 km depth because both *P* and *S* velocity heterogeneities are of lower amplitude and more random appearance in the lower mantle compared to the upper mantle. Especially for *S* waves the resolution is unsatisfactory in many places below 800 km. Laterally, the slab appears to buckle at several locations in the upper mantle, probably due to geometrical convergence similar to that proposed by *Minamino and Fujii* [1981]. There are apparently three major segmentations of the slab, as shown in horizontal slices in the depth range 400-450 km in Figure 8. These segmentations are under the junctions of the Kurile, Japan, Izu-Bonin, and Mariana trenches and all correlate with abrupt lateral changes in the Wadati-Benioff zone. The central portion of the Kurile slab anomaly is torn apart near the bottom of the upper mantle.

To illustrate the vertical morphology of the slab, a series of vertical slices of the *P* wave image in the 2°x2°x50 km grid across the strike of subduction zones, paired with results of some impulse tests for resolution, are shown in Figure 10. The results of the impulse tests are used to judge the reliability of the image at various locations and, particularly, to detect any along-path smearing. Similarly, the interpretation of the seismic slab model for the region (Figure 9), although based on horizontal slices, also uses the impulse tests results. To display more stable and representative anomalous patterns, we stacked, *i.e.*, averaged, series of parallel vertical slices in areas where the subduction zone is relatively straight. Some of these stacked profiles of the images in the 1°x1°x50 km grid are shown in Figure 11, with their surface locations shown in the small boxes in Figure 1.

In the stacked *P* wave slices in Figure 11, some focal mechanism solutions are plotted, in the plane of the vertical slice. As listed in Table 2, these mechanisms are mainly from the centroid moment tensor (CMT) solutions by *Dziewonski and Woodhouse* [1983], *Giardini* [1984], and *Dziewonski et al.* [1983*a-c*, 1984*a-c*, 1985*a-d*, 1986*a-c*, 1987*a-g*, 1988*a-f*] of events deeper than 100 km and from *Isacks and Molnar* [1971] and *Oike* [1971]. The principal axes of most mantle events follow the downdip direction of the high-velocity slab and seismicity, the latter in agreement with the observation by *Isacks and Molnar* [1971]. The depth at which compression begins to dominate the downdip stress regime in the slab apparently depends on the dip and bending of the slab in this region. This depth is below 350 km under the Mariana arc where the slab dip is nearly vertical; around 300 km under the Kuriles where the slab dip is steep; around 200 km under Japan where the slab dip is shallow; and shallower than 150 km under the Izu-Bonin arc where the slab bends to subhorizontal near the bottom of the upper mantle.

In the cross sections, the fast slablike anomalies which are associated with subduction zone seismicity become contorted and broadened with depth. This suggests that the slab is encountering a resistance. The thickness of the resolvable slab anomaly is bounded below by the size of the inversion blocks. The maximum thickness of the slab anomaly which we resolved is about 100-200 km, while the real slab could be much thinner. The slab related anomalies extend to 650 km depth in most areas of the region. Fingering of the slab, *i.e.*, segmenting and spreading, is apparent in some places in the images resolved in the transition zone depth range. Although along-path smearing of fast anomalies sometimes causes artificial fingering, we observed fingerings in regions of good resolution. For instance, the fast slab anomaly under the southern part of the Izu-Bonin arc has a consistently high dip, while the slab anomaly bends arcward to subhorizontal under the central and northern part of the arc (profile D-D1 in Figures 10 and 11). Distribution of deep seismicity in the region shows the same pattern. Fast velocity anomalies in the form of single coherent sheets are not evident in the lower mantle of the region.

Under the Kuriles (slice A-A1) the fast slablike anomalies appear contorted, and fingering is seen around 600 km. The deepest fast slab anomaly reaches to 700 km, but the deep resolution for amplitude is quite poor (see the right panel of Figure 10*a*). In an early inversion, without the grouping and sorting procedure discussed in section 2, the apparent resolution was good to depths greater than 900 km, but the noise level was much higher. A fast anomalous band to depth near 850 km was seen. The current work shows that the issue of deep slab penetration in this region cannot be resolved. However, our inversions with and without the grouping and sorting procedure indicate that the maximum depth of a fast anomaly in this region is probably between 700 km and 850 km. We do not know the depth of the 670-km discontinuity in this region. It can be very deep in subduction zone regions, particularly if it is a chemical boundary.

The slab under Japan (profiles B-B1 and C-C1) has a relatively constant low dip angle, which flattens to subhorizontal near the 670-km discontinuity. Even though there are no earthquakes below 450 km along slice B-B1, a fast slab is seen extending to the upper mantle-lower mantle boundary. The resolution of the image is very sharp in this area (see B-B1 and C-C1 in Figure 10). In the lower portion of the upper mantle along slice C-C1, stacked *P* wave profile of Figure 11*c* shows a slow region coinciding with an intense cluster of deep-focus seismicity. The fast slablike anomaly in the profile has a steeper dip angle than the Wadati-Benioff zone. A similar picture was observed by *Kamiya et al.* [1988] in their central Japan profile. On the other hand, the fast slablike anomaly in the stacked *S* wave profile of Figure 11*c* is almost parallel with the seismicity trend. In fact, an unstacked profile in the region (Figure 10*c*) shows two fast velocity trends near the bottom of the upper mantle, one follows the seismicity trend, while the other extends to the lower mantle with a steeper dip angle, and both eventually flatten to subhorizontal. The deep fast slab anomaly in the region by *Kamiya et al.* [1988] has an even steeper dip which, as discussed by *Zhou* [1988], is perhaps caused by the use of a large amount of teleseismic data and associated along-path smearing (see Figure 3 of *Kamiya et al.* [1988]). Two factors make the fast trend which is associated with deep-focus seismicity more believable, *i.e.*, (1) it follows the interpreted model which is based on the more stable patterns in map views. The subduction zone curves in the stacked region (C-C1 in Figure 1) making the stacked result less stable here than in other regions; (2) it follows the location of deep-focus seismicity and, in particular, the compressional direction of the focal mechanisms (Figure 11*c*). If this fast trend really represents the major subduction direction of the area, the subducted Pacific lithosphere probably slips from underneath Japan into a subhorizontal attitude under the edge of the Asian continent. The presence of different fast velocity trends, as seen in this area of good resolution, supports the possibility of slab fingering.

Bending near the bottom of the upper mantle is apparent in both seismicity and the slablike anomaly under most parts of the Izu-Bonin arc (slice D-D1). The slab is steeply dipping above 400 km but becomes subhorizontal somewhat below the deepest earthquakes. As mentioned above, fingering of the deep slab anomalies is apparent in this region. The deepest portion of the slab model in this slice is probably unreliable, since there is no clear indication of fast anomalies in the model slab location. Finally, both horizontal and downward spreading of the high-velocity anomaly is indicated in the Mariana subduction zone (E-E1), although the resolution is poor in parts of this region. Thickening and flattening of the slab are possible. Some fast anomalies are seen around 900-1000 km depth, in the form of horizontal layers which are separated by slow layers above and below. Many of the anomalies mentioned above are verified by resolution tests, although further investigation is needed on the existence of any systematic noise which may cause artifacts.

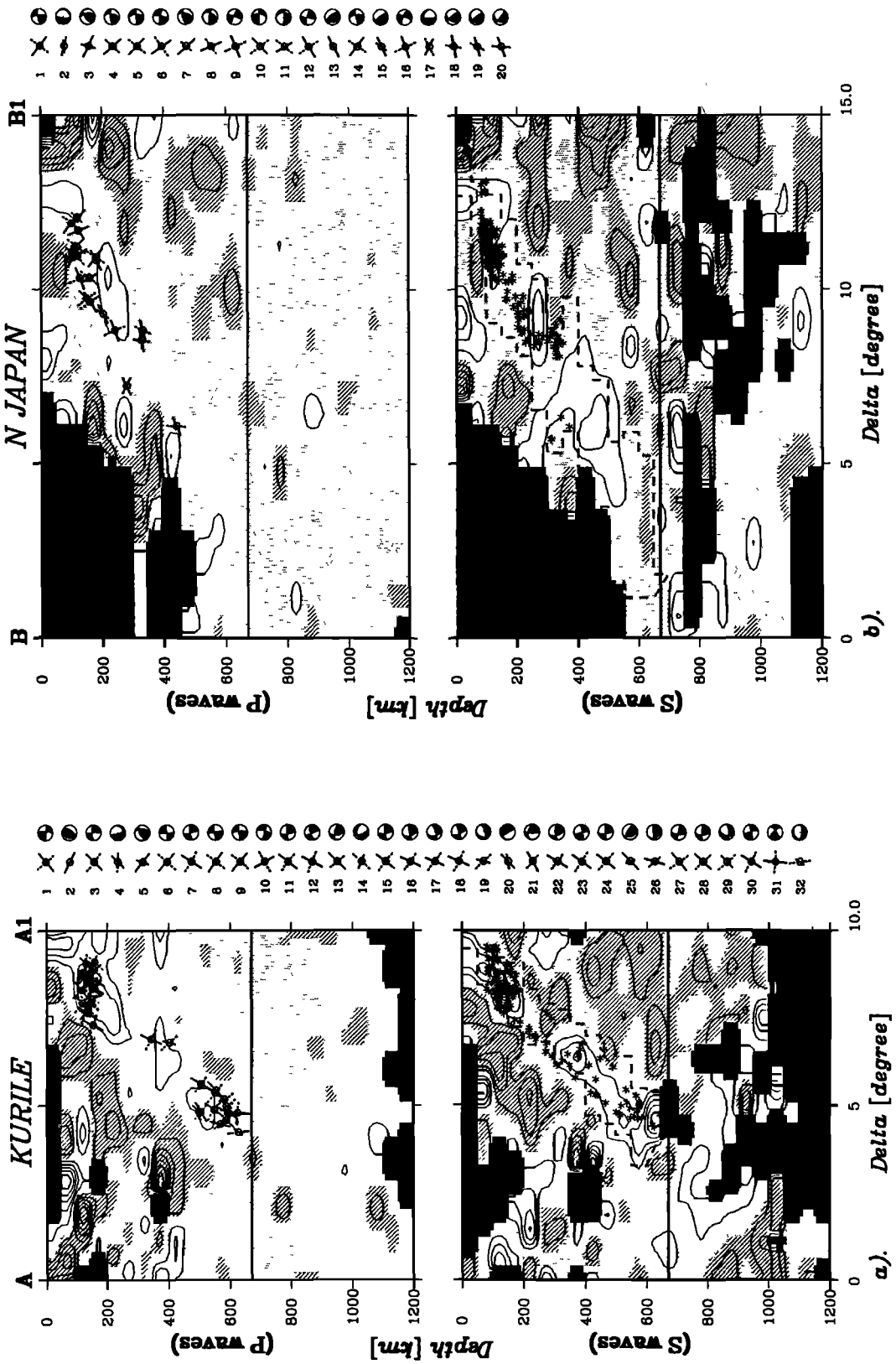
KURILE
A
A1
N JAPAN
B
B1
(P WAVES)
(S WAVES)
Depth [km]
Delta [degree]
a).
b).

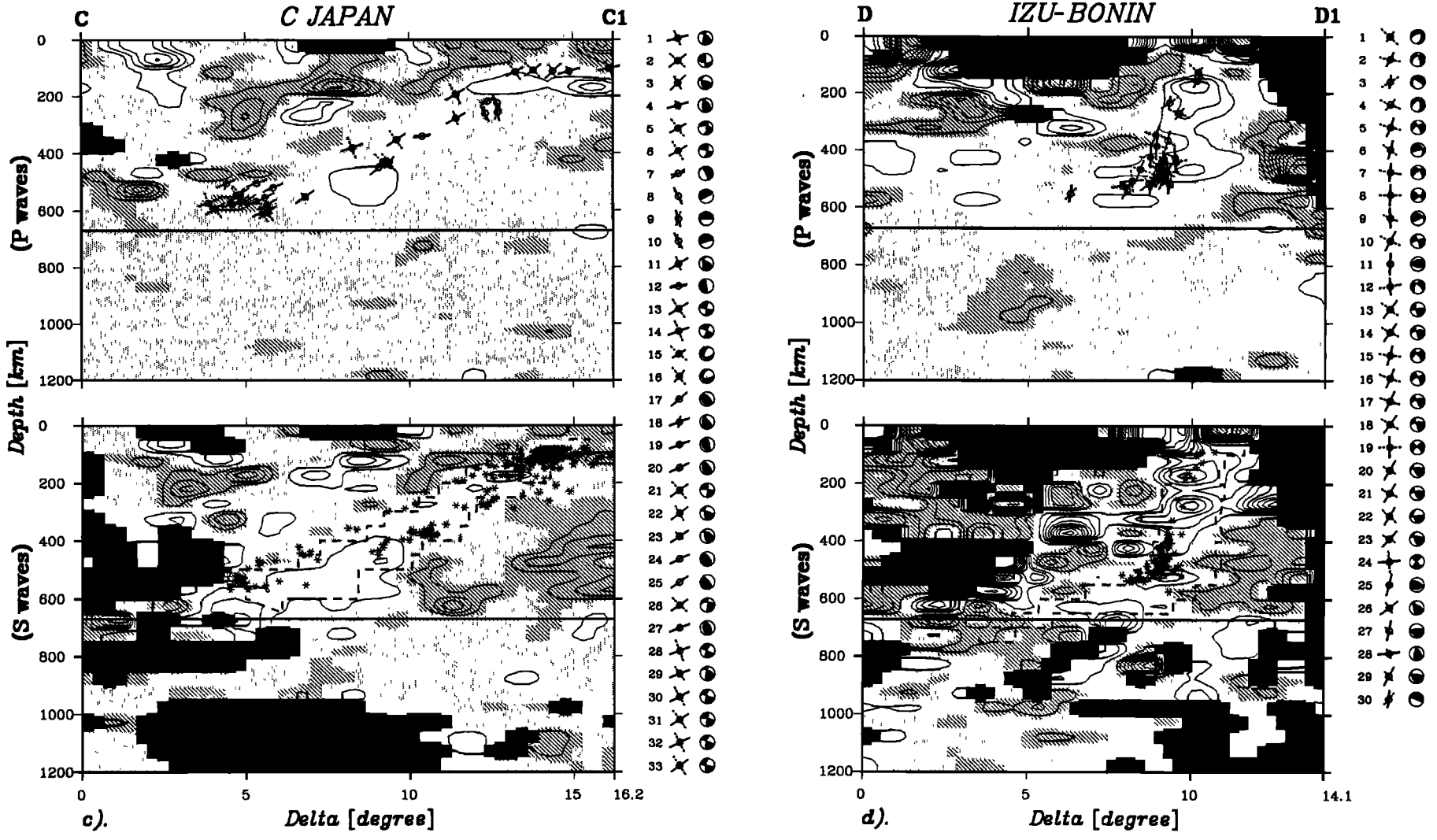

Fig. 11. Stacked vertical slices on 1°x1°x50 km grid. The locations of these stacked slices are indicated as the small boxes in Figure 1. Each pair of slices are the *P* (top) and *S* (bottom) wave images, respectively. The plotting convention follows that used in Figure 10. The heavy dashed lines in the *S* wave slices indicate the cross section of the interpreted slab model along the center slice stacked. In the *P* wave slices, instead of earthquake foci, focal mechanism solutions from some previous studies (see Table 2) are plotted. Each solution is plotted as an equal-area projection of the "lower hemisphere" onto the cross section. The solutions plotted inside each panel are principal stress axes, with dashed *T* axes and solid *P* axes. An axis reaches to a maximum length if it is exactly on the slice. Both principal stress axes and nodal plane plots, in ascending order of focal depths, are given to the right of each panel. Notice that most of the compressional axes consistently follow the downdip directions of the fast slablike anomalies. (*a*) Kurile, (*b*) north Japan, (*c*) central Japan, (*d*) Izu-Bonin, and (*e*) Mariana.

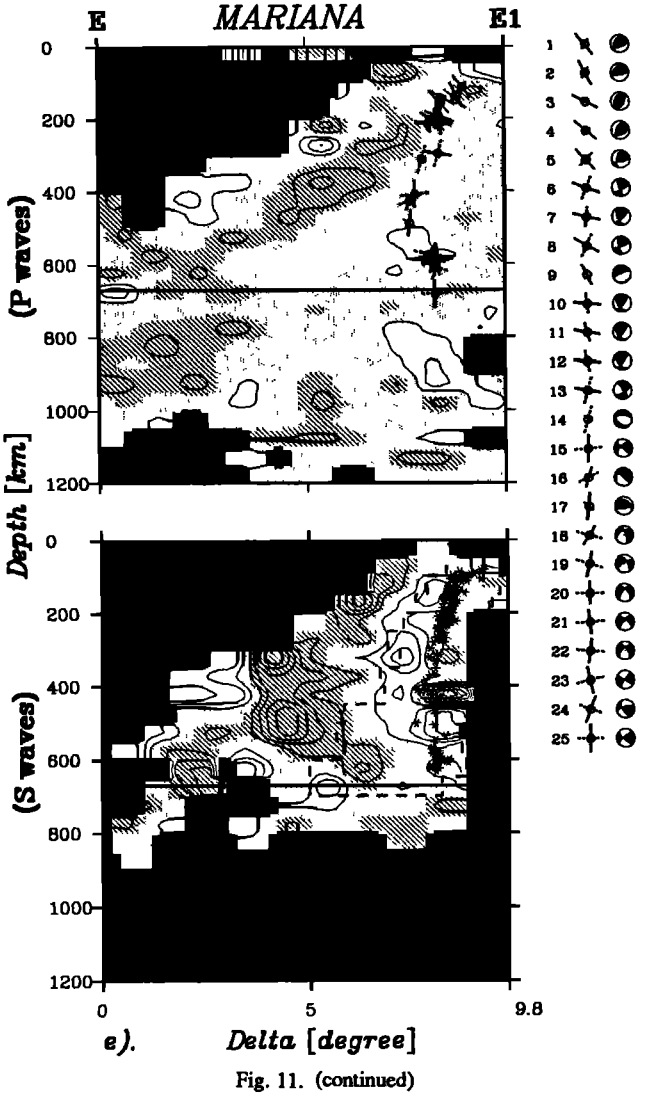

Fig. 11. (continued)

Slow velocity anomalies on the arcward and trenchward sides of the slabs in the upper part of the upper mantle are clearly shown in the results. One of the largest slow anomalies imaged is under the back arc region of the northern Phillippine plate, extending north to underneath the Sea of Japan (see the 200-250 km panels in Figures 7 and 8 and vertical slices C-C1 and D-D1 in Figures 10 and 11). This anomaly occurs from the near surface down to almost 300 km in depth, coincident with the anomalous absence of seismic activity in the same area below 70 km. Away from the deep subduction zones, shallow fast slab anomalies are also resolved under Luzon and Ryukyus, extending farther north, along the east edge of the Sea of Japan (Figures 7 and 8). In the following discussion, however, we will concentrate on structures under the major subduction zones of the northwest Pacific.

6. DISCUSSION

The depth extent of the subducted lithosphere, the first basic question in our introduction, is a critical and difficult problem. Although this study yields high resolution images of the fast slablike anomaly, the question is still largely open, mainly due to the nonuniqueness in interpretation and the decrease of amplitude resolution at depth. Penetration of lithospheric slab into the lower mantle has been proposed previously for the region based on residual sphere studies [*Jordan*, 1977; *Creager and Jordan*, 1984, 1986]. A deep anomaly has been found in the Kurile region from a waveform analysis [*Silver and Chan*, 1986]. Our study involves earthquakes in a large region and utilizes rays from other sources which traverse the mantle below the earthquakes. The inverse approach we use makes no assumptions about the form of the anomaly. On the other hand, forward modeling is a logical check on the inversion results [e.g., *Zhou et al.*, 1990]. It should be pointed out that since residual sphere studies have essentially zero resolution along the ray paths, the anomaly could generally be anywhere between the source and the receiver.

Our images indicate that fast slablike anomalies appear to extend to below 670 km in parts of the Mariana subduction zone and possibly parts of the Kurile subduction zone (slices E-E1 and A-A1 in Figures 10 and 11). The slab in other places, however, tends to flatten to subhorizontal around 600 km depth, in accordance with flattening in the seismicity. The difficulty in making a general interpretation of the slab is apparent. There are apparently many fast regions in the upper part of the lower mantle that are unrelated to Wadati-Benioff zones and other regions where the deepest earthquakes are underlain by slow anomalies in the lower mantle. In many cases, because we do not know if the 670-km discontinuity is elevated or depressed, we do not know if the velocity anomaly, or the inferred lithosphere, crosses the discontinuity.

According to *Hager and Raefsky* [1981], an accumulation of old slab would lead to a depression of the 670-km discontinuity by at least 25 km and would likely reach 150 km if the mantle is chemically layered. From this system to whole mantle convection on the other end, the degree of depression is expected to be smaller. Observationally, a sharp 670-km discontinuity has previously been suggested based on precursors to *P'P'*, denoted by *P'670P'* [e.g., *Engdahl and Flinn*, 1969; *Whitcomb and Anderson*, 1970; *Richards*, 1972; *Husebye et al.*, 1977; *Nakanishi*, 1988]. However, it is important to mention that *P'670P'* phases are not consistently observed and the erratic nature of them suggests extreme lateral heterogeneity in the 670-km discontinuity [*Nakanishi*, 1988; *Wallace and Holt*, 1988]. *Barley et al.* [1982] and *Faber and Müller* [1984] discussed converted phases and suggested that they are scattered from lateral heterogeneity around 650 km depth. Faber and Müller pointed out that a relatively smooth transition zone between the upper mantle and lower mantle below East Asia can explain the lack of precursor energy for events in and close to Japan. *Bock and Ha* [1984] found a large *S-P* phase conversion depth (~700 km) under Tonga, which may result from a dynamical or thermal deformation of the 670-km discontinuity beneath the Tonga slab. In this study, correlations between adjacent panels appear much poorer across a depth around 650 km (Figure 8). This suggests that if slabs do cross the 670-km discontinuity, they likely do not retain the form of a single coherent sheet but exist in the form of either small fingers or very broad patches. But this is not consistent with the proposal of *Creager and Jordan* [1984, 1986].

Previous theoretical and experimental studies [e.g., *Anderson*, 1979, 1987*a*; *Knittle et al.*, 1986; *Kincaid and Olson*, 1987; *Ringwood and Irifune*, 1988] give varying results on the relative buoyancy of the slab near the upper mantle-lower mantle boundary. *Anderson* [1979, 1987*a*] points out that both peridotite and eclogite are less dense than the lower mantle and slabs may therefore be unable to penetrate the boundary, although boundary deformation is possible. Fast regions in the lower mantle may be due to thermal coupling, *i.e.*, cooling of the lower mantle by the slab. This adds extra difficulty to interpreting deep slab morphology from tomographic images. Flattening of the slab could be a result of either chemical or viscous stratification. A deep extension of a fast anomaly could be the result of local penetration or thermal coupling. The images indicate that morphology of the slab in the transition region is apparently very complicated. The possible fates of the slab has been discussed in

TABLE 2. Earthquake Focal Mechanisms Used in Figure 11

No.	Date	Latitude, °N	Longitude, °E	Depth, km	m_b	*T* Axis		*P* Axis		Reference
						δ, deg	θ, deg	δ, deg	θ, deg	
				Kurile (A-A1)						
1	Sept. 3, 1978	48.94	154.76	117.6	5.5	47	150	41	311	CMT
2	Dec. 10, 1977	47.29	153.12	119.0	5.2	15	219	26	121	CMT
3	Feb. 2, 1986	48.43	153.17	119.2	5.3	38	114	45	331	CMT
4	Sept. 23, 1987	45.70	149.57	130.9	—	3	192	31	283	CMT
5	July 20, 1979	47.15	152.72	132.1	5.2	30	37	37	154	CMT
6	Oct. 30, 1983	47.57	153.01	133.7	—	49	309	41	132	CMT
7	March 22, 1972	49.06	153.57	134.0	6.8	30	114	58	311	SM
8	Dec. 1, 1967	49.50	154.40	136.0	—	51	325	36	117	IM
9	Jan. 29, 1963	49.70	155.00	143.0	—	48	328	40	122	IM
10	May 30, 1985	48.76	153.96	150.7	5.5	31	316	57	159	CMT
11	July 19, 1986	47.05	151.32	153.4	5.9	34	114	53	322	CMT
12	Aug. 22, 1984	49.23	153.08	153.8	5.2	21	108	63	327	CMT
13	June 19, 1977	46.38	151.19	157.4	5.6	37	94	44	317	CMT
14	Jan. 29, 1978	45.65	149.57	159.0	5.5	46	358	14	103	CMT
15	Dec. 20, 1977	47.81	153.12	159.1	5.8	37	116	53	305	CMT
16	July 8, 1987	46.23	149.53	159.4	—	30	117	59	290	CMT
17	Aug. 17, 1961	46.40	149.30	160.0	6.7	35	130	50	275	FK
18	July 10, 1978	48.27	150.18	343.7	5.1	25	123	64	291	CMT
19	June 21, 1978	47.98	149.01	402.0	5.9	44	121	35	253	CMT
20	Sept. 1, 1965	51.29	150.70	501.0	—	7	252	35	347	Oi
21	June 4, 1984	51.20	150.61	505.6	5.2	30	76	29	327	CMT
22	Jan. 4, 1987	49.53	149.51	505.4	5.1	28	96	58	308	CMT
23	Dec. 30, 1979	52.38	151.90	548.7	5.4	33	115	54	270	CMT
24	May 18, 1987	49.12	147.39	551.7	6.0	38	140	52	320	CMT
25	Jan. 29, 1982	49.15	147.85	553.8	5.2	21	73	44	321	CMT
26	June 10, 1980	51.49	150.27	569.1	5.2	30	61	60	242	CMT
27	Feb. 1, 1984	49.10	146.31	581.3	6.0	50	133	39	328	CMT
28	Jan. 25, 1979	50.38	148.63	587.6	5.4	41	106	47	306	CMT
29	July 14, 1987	49.59	147.67	588.6	—	51	142	30	279	CMT
30	April 20, 1984	50.19	148.77	592.8	6.0	29	154	60	323	CMT
31	Aug. 30, 1970	52.36	151.73	625.0	—	5	130	85	310	ST
32	Nov. 27, 1982	50.22	147.01	628.0	5.6	68	82	22	261	CMT
				N Japan (B-B1)						
1	March 10, 1985	43.20	145.81	101.2	5.3	49	340	37	129	CMT
2	Sept. 12, 1981	42.70	143.31	105.3	4.9	12	167	3	258	CMT
3	June 21, 1984	42.46	142.48	106.5	5.5	37	38	24	148	CMT
4	March 6, 1984	42.53	142.83	106.2	5.5	37	5	48	153	CMT
5	May 29, 1982	42.46	143.20	118.1	5.7	49	345	41	164	CMT
6	Jan. 23, 1981	42.20	142.07	120.9	6.3	35	335	55	146	CMT
7	Dec. 10, 1985	43.76	146.90	120.0	5.3	26	7	46	127	CMT
8	Feb. 18, 1980	43.42	145.72	124.3	5.4	28	350	62	163	CMT
9	May 21, 1964	42.90	141.90	129.0	—	64	120	22	333	Oi
10	Dec. 6, 1985	43.10	140.86	152.1	5.1	50	170	40	355	CMT
11	July 4, 1967	43.20	142.50	160.0	—	45	356	43	193	IM
12	Aug. 20, 1966	43.10	140.60	163.0	—	53	120	33	328	IM
13	Dec. 6, 1978	44.74	145.82	181.0	6.7	18	22	28	282	CMT
14	Oct. 25, 1965	44.20	145.30	181.0	—	50	346	36	139	IM
15	Jan. 19, 1969	45.00	143.20	204.0	6.5	28	16	22	274	Cn
16	June 21, 1979	43.63	139.63	241.5	5.4	65	125	20	344	CMT
17	May 31, 1981	44.72	137.77	280.8	5.4	22	7	19	104	CMT
18	July 14, 1982	45.62	142.57	328.7	—	43	28	11	287	CMT
19	Jan. 6, 1985	45.56	143.06	332.5	5.3	38	14	14	273	CMT
20	May 7, 1987	46.67	139.01	442.2	6.1	53	38	18	283	CMT

TABLE 2. (continued)

No.	Date	Latitude, °N	Longitude, °E	Depth, km	m_b	*T* Axis δ, deg	*T* Axis θ, deg	*P* Axis δ, deg	*P* Axis θ, deg	Reference
				C Japan (C-C1)						
1	Nov. 17, 1977	33.64	140.40	103.6	5.5	42	59	14	315	CMT
2	July 28, 1985	37.20	140.52	109.0	5.3	41	145	36	275	CMT
3	Oct. 4, 1985	35.52	139.74	113.7	5.8	37	57	44	281	CMT
4	Aug. 12, 1982	34.25	139.03	113.0	5.3	23	50	16	313	CMT
5	Oct. 7, 1985	38.02	140.41	114.8	5.1	54	101	25	330	CMT
6	July 27, 1965	40.21	139.36	195.0	—	60	125	30	306	Oi
7	March 4, 1959	37.60	138.70	219.0	—	7	246	23	350	Ic
8	May 14, 1954	36.00	137.40	225.0	—	29	198	49	71	Ri
9	Oct. 8, 1978	35.95	137.35	257.6	5.3	39	234	51	55	CMT
10	Nov. 14, 1986	35.98	136.72	261.7	5.1	37	213	46	70	CMT
11	May 28, 1979	37.33	136.82	279.3	5.1	37	48	31	292	CMT
12	Feb. 3, 1982	36.83	134.28	341.6	5.4	1	184	9	274	CMT
13	March 11, 1984	38.54	135.09	353.8	5.3	57	132	33	301	CMT
14	Oct. 21, 1978	41.31	135.41	380.9	5.1	69	96	20	297	CMT
15	March 6, 1978	38.34	134.12	430.1	5.1	42	145	22	256	CMT
16	Jan. 18, 1980	37.64	133.52	432.5	5.5	52	115	31	255	CMT
17	May 31, 1935	38.60	134.20	450.0	—	7	27	41	291	Hi
18	Feb. 3, 1977	42.59	130.49	504.7	5.0	30	16	21	274	CMT
19	Feb. 11, 1987	43.13	132.16	504.2	5.4	6	177	21	269	CMT
20	Sept. 28, 1983	41.42	131.78	519.9	5.1	18	21	24	283	CMT
21	Dec. 25, 1979	42.93	131.33	543.0	5.0	52	97	36	299	CMT
22	Nov. 27, 1981	42.88	131.12	546.2	5.7	42	48	38	274	CMT
23	Dec. 11, 1964	38.90	130.22	551.0	—	18	73	34	330	Oi
24	Aug. 6, 1965	41.39	131.34	554.0	—	14	20	26	283	Oi
25	April 10, 1969	42.02	131.07	564.0	—	17	10	32	268	ST
26	April 15, 1984	42.73	131.24	566.8	5.0	39	79	32	319	CMT
27	Sept. 9, 1977	42.59	131.86	567.7	4.9	7	15	22	282	CMT
28	Oct. 8, 1983	44.18	130.39	572.8	5.7	70	80	20	261	CMT
29	Jan. 31, 1979	42.92	130.95	575.2	5.7	38	49	21	301	CMT
30	March 9, 1977	41.48	131.55	578.6	5.9	58	86	29	295	CMT
31	Jan. 3, 1957	43.80	130.60	593.0	—	55	86	33	287	Hi
32	Aug. 16, 1979	41.97	131.74	604.4	6.1	59	76	26	294	CMT
33	Oct. 8, 1960	40.20	130.00	605.0	—	56	118	34	298	Hi
				Izu-Bonin (D-D1)						
1	Dec. 11, 1979	28.81	140.83	124.7	6.1	44	74	25	317	CMT
2	Sept. 6, 1982	29.18	140.65	155.6	6.6	11	51	39	312	CMT
3	April 16, 1980	27.90	140.07	231.8	5.4	30	221	38	338	CMT
4	March 15, 1978	26.22	140.65	270.1	6.1	23	70	30	326	CMT
5	May 21, 1977	27.28	139.72	345.2	5.1	15	64	62	302	CMT
6	Jan. 14, 1979	29.08	139.60	363.9	4.9	29	111	59	311	CMT
7	Dec. 16, 1980	28.34	139.48	384.2	5.3	11	77	56	331	CMT
8	Sept. 7, 1979	27.84	139.40	422.9	4.9	0	89	81	180	CMT
9	Dec. 3, 1985	26.90	140.44	425.4	6.1	16	129	68	356	CMT
10	May 13, 1977	28.12	139.73	439.7	5.8	25	60	60	275	CMT
11	Nov. 17, 1984	28.35	139.72	439.7	5.3	6	175	84	324	CMT
12	Sept. 8, 1982	26.76	140.49	441.4	5.4	11	252	52	357	CMT
13	March 5, 1984	28.86	139.34	455.6	5.1	35	38	54	236	CMT
14	April 3, 1985	28.40	139.61	455.1	5.9	24	36	55	265	CMT
15	March 17, 1986	27.37	139.81	457.7	5.5	7	61	60	318	CMT
16	June 23, 1982	29.03	138.59	466.8	—	19	57	60	290	CMT
17	Oct. 4, 1985	27.56	139.82	467.7	5.6	16	49	61	287	CMT
18	July 11, 1951	28.10	139.90	475.0	—	26	37	53	268	Ri
19	Dec. 11, 1980	26.33	140.23	475.9	5.3	1	256	77	350	CMT
20	May 10, 1978	27.77	139.68	493.8	5.0	18	19	60	255	CMT
21	Sept. 10, 1985	27.14	139.91	496.9	5.8	21	35	60	263	CMT
22	May 21, 1984	26.80	140.07	504.9	5.0	35	42	55	223	CMT
23	March 3, 1965	28.12	139.51	507.0	—	20	18	48	255	Oi
24	Jan. 17, 1980	28.24	138.62	507.0	5.3	84	38	5	241	CMT
25	Sept. 5, 1985	28.00	139.40	515.5	4.9	2	324	76	228	CMT
26	Feb. 3, 1986	27.84	139.34	516.0	5.7	28	1	38	247	CMT
27	Oct. 14, 1982	27.15	140.23	517.1	5.1	20	8	70	196	CMT
28	March 19, 1987	29.26	137.80	524.0	5.3	24	342	7	249	CMT
29	Dec. 29, 1977	28.50	138.34	538.4	5.2	24	358	58	220	CMT
30	July 4, 1982	27.92	136.48	551.8	6.3	32	189	50	326	CMT

TABLE 2. (continued)

No.	Date	Latitude, °N	Longitude, °E	Depth, km	m_b	*T* Axis δ, deg	*T* Axis θ, deg	*P* Axis δ, deg	*P* Axis θ, deg	Reference
				Mariana (E-E1)						
1	May 2, 1985	19.05	145.97	113.4	5.1	21	179	52	60	CMT
2	Jan. 2, 1965	19.10	145.80	136.0	—	22	177	60	43	KS
3	May 9, 1987	19.06	145.42	144.4	5.2	2	158	28	67	CMT
4	Sept. 14, 1983	18.07	145.96	148.4	6.0	12	187	42	85	CMT
5	April 7, 1982	18.93	145.42	157.0	—	28	194	48	68	CMT
6	Sept. 9, 1978	18.42	145.47	193.0	5.2	56	202	19	82	CMT
7	Dec. 18, 1978	18.45	145.42	200.9	5.2	46	174	13	69	CMT
8	Oct. 14, 1981	18.24	145.35	202.5	5.0	55	207	29	65	CMT
9	May 25, 1985	17.40	145.60	205.6	5.3	47	144	33	9	CMT
10	May 24, 1977	18.36	145.51	206.1	5.7	47	161	6	64	CMT
11	April 14, 1985	18.90	145.10	214.4	5.0	41	151	9	54	CMT
12	May 13, 1979	18.79	145.42	215.6	5.9	48	152	4	58	CMT
13	April 13, 1986	17.18	145.57	296.7	5.1	71	230	9	111	CMT
14	June 7, 1981	16.64	145.15	311.8	5.7	73	247	10	15	CMT
15	July 24, 1977	19.30	144.62	409.1	5.4	5	230	74	338	CMT
16	Dec. 27, 1986	20.08	144.17	425.9	5.1	20	201	47	314	CMT
17	Aug. 15, 1978	19.74	144.31	488.9	5.4	17	134	73	317	CMT
18	Dec. 25, 1979	18.44	145.16	576.0	5.4	15	58	41	314	CMT
19	Oct. 30, 1979	18.68	145.27	578.7	5.6	17	89	64	322	CMT
20	Oct. 17, 1979	18.54	145.30	583.8	6.1	0	260	55	350	CMT
21	May 10, 1970	18.62	145.41	587.0	—	4	261	66	4	ST
22	Feb. 27, 1977	18.21	145.30	592.6	5.0	4	75	60	337	CMT
23	Jan. 4, 1982	17.92	145.46	595.2	6.1	13	256	77	78	CMT
24	Dec. 27, 1982	19.64	145.07	608.8	5.3	16	32	70	249	CMT
25	March 7, 1962	19.10	145.20	683.0	—	0	49	90	49	KS

Events in each area are in ascending order of their focal depthes. If a *T* or a *P* axis is along the downdip direction of the slab, its plunge (δ) and azimuth (θ) angles are underlined. The references are CMT, *Dziewonski and Woodhouse* [1983], *Giardini* [1984], and *Dziewonski et al.* [1983*a-c*, 1984*a-c*, 1985*a-d*, 1986*a-c*, 1987*a-g*, 1988*a-f*]; Cn, *Chandra* [1971]; FK, *Fujita and Kanamori* [1981]; Hi, *Hirasawa* [1966]; Ic, *Ichikawa* [1966]; IM, *Isacks and Molnar* [1971]; KS, *Katsumata and Sykes* [1969]; Oi, *Oike* [1971]; Ri, *Ritsema* [1965]; SM, *Stauder and Maulchin* [1976]; and ST, *Sengupta and Toksöz* [1977].

many studies [e.g., *Davies*, 1980; *Vidale*, 1987; *Gurnis and Hager*, 1988]. It is therefore not adequate to extrapolate the general characteristics of the slab from observation in a few places only. For instance, even if the slab indeed descends into the lower mantle under the Kuriles, the calculation of the total downward flux across the boundary based on this result would obviously be too large, since the high-velocity anomaly is not continuous across the boundary in many other places. Our study also shows that it is not appropriate to take the magnitude of the slab related anomaly from shallow and intermediate depth earthquakes and apply it to deep-focus earthquakes. More detailed studies of all subduction regions are needed to advance our understanding about the slab penetration issue.

To the second and third basic questions, our study has illustrated many aspects of the vertical and lateral morphology of the slab. Along the strike of the slab, our images suggest that most slab anomalies under island arcs of the northwest Pacific are continuous but become contorted and broadened with depth. This indicates that the descending lithosphere is initially quite coherent. On the other hand, as suggested in our interpreted model in Figure 9, segmentation of the major northwest Pacific slab, which is under the Kurile, Japan, Izu-Bonin, and Mariana arcs, takes place below 400 km depth. The segmentation may partially be a consequence of along-strike stretching due to differential flattening on different slab segments. In our interpreted slab model, the along-strike length of the major northwest Pacific slab between 13°N and 51°N increases about 15% from the surface to 400 km depth if ignoring truncations of the slab. This estimation can also be make simply from the lateral trace of seismicity at those depths. If along-strike stretching and across-strike broadening of the lithospheric slab really occurs, the descending velocity of the slab should decrease.

Contortion and flattening seem to be a general characteristic of the vertical morphology of the slab in the upper mantle. The slab probably thickens with depth and is fingered and broadened to several times its near-surface thickness in the transition zone. This slab broadening phenomena, if real, is obviously not just a thermal conduction effect. Temperature induced phase changes [*Anderson*, 1987*a*], increase in viscosity with depth [*Gurnis and Hager*, 1988] and slab doubling [*Giardini and Woodhouse*, 1984] are large effects. Piling up of the slab material around the boundary is another hypothesis [*Anderson*, 1987*a*]. These effects seem to be in accord with the peak of deep seismicity below 350 km and the downdip compressional stress regime of the slab as suggested by focal mechanisms of deep earthquakes [*Isacks and Molnar*, 1969, 1971].

It is well known that in the downdip direction subducted lithospheric slabs are generally in extension above 300 km depth and in compression below, as inferred from the principal stress axes of mantle earthquakes [*Isacks and Molnar*, 1969, 1971]. We have compared our images of the slab with some existing focal mechanism solutions (Table 2 and Figure 11) in the region. The compressional axes of most deep events consistently follow the downdip direction of the seismic slab, even when the slab bends to

subhorizontal at depth (Figure 11d). The depth at which compression begins to dominate the downdip stress regime in the slab apparently depends on the topology of the slab in this region. This depth may also relate to the age since subduction initiated.

Since the principal stress axes are generally well constrained, the agreement between the principal compression and downdip directions of the slab is a strong one. If this relation is generally true, *i.e.*, if the slab functions as a stress guide, the orientations of the compressional axes of mantle earthquakes can be used to infer the downdip direction of the slab in a tomographic image. For instance, our images imply that the slab under Japan subducts with a small dip angle to regions beneath continental Asia, and the slab under the Izu-Bonin arc bends to subhorizontal; if the above assumption is right for those areas, the anomalies are probably the true signals of the slab because they are consistent with the observed directions of the compressional axes.

In most cases, the resolved slab anomalies are associated with clusters of seismic activity. There are indications that the peaks of deep seismicity tend to spatially coincide with either flattening or fingering of the slab-related anomalies. Most shallow earthquakes occur near the top of the lithospheric slab [e.g., *Engdahl and Gubbins*, 1987] due to bending of the oceanic plate and breaking of interplate asperities [*Lay and Kanamori*, 1981]. From this study, however, we find that hypocentral locations in the lower half of the upper mantle sometimes lie nearer the central or even the bottom parts of the fast anomalies. Source location uncertainty does not affect this observation greatly since the fast slab anomalies are resolved with respect to the given source locations and the location uncertainty is small for most events used. This means that the dips of Wadati-Benioff zones, as determined from earthquake locations, can be independent of the slab dips inferred from the fast velocity anomalies. The shallow dips of the earthquakes, assumed to represent the slab, have been used to argue for whole mantle convection and deep slab penetration [e.g., *Hager and O'Connell*, 1981].

Our observations support the hypothesis that the descending lithospheric slabs finger and spread above or near the upper mantle-lower mantle boundary. This, plus the peaks of deep seismicity, appears to be the consequence of the slab encountering a barrier of some form around the transition zone. This could be associated with an increase in viscosity [e.g., *Hager*, 1984; *Hager et al.*, 1985], a chemical or intrinsic density contrast, or the loss of negative buoyancy of the slab [*Anderson*, 1979, 1984; *Jeanloz and Thompson*, 1983; *Anderson and Bass*, 1986]. Observations of deep seismicity and source mechanisms in the Tonga subduction zone by *Giardini and Woodhouse* [1984, 1986] appear unfavorable to slab penetrating the 670-km discontinuity, and these authors propose that the deepest part of the slab is displaced laterally by shear flow in the mantle. Travel time analyses in Tonga by *Sondergeld et al.* [1977], *Bock* [1981], and *Ansèll and Gubbins* [1986] found no indications for high seismic velocities in the deeper parts of the subducting slab, but their view is challenged by other workers [*Fitch*, 1977; *Frohlich and Barazangi*, 1980; *Fischer et al.*, 1988], who suggested the presence of 5-10% high-velocity anomalies at depths below 600 km.

The compressional and shear velocities obtained in this study agree well with some previous works in the northwest Pacific region. For instance, comparison with five cross sections from a regional least squares inversion by *Hirahara* [1981] indicates good correlation exist with four of them, with the one under Kinki to Kii being the exception. Under the southern part of the Sea of Japan and central Honshu, a slow anomaly from the near surface to about 300 km depth was previously detected [*Hirahara*, 1977, 1981; *Hirahara and Mikumo*, 1980]. This is part of a large slow feature resolved in this study (Figures 7, 11*b*, and 11*c*). This feature extends to the Phillippine plate and coincides with the absence of intermediate to deep earthquakes in parts of the region. These results are obtained from different inversion methods on different blocks, from similar data.

In a recent survey of intermediate and deep seismicity in the Circum-Pacific region, *Burbach and Frohlich* [1986] have located four well-constrained possible segmentation boundaries (PSBs) along the Kurile, Japan, Izu-Bonin, and Mariana trenches. They have also noticed the abnormal absence of deep seismic activity around two of their PSBs at the junctions of the Kurile and Japan trenches and Japan and Izu-Bonin trenches. Our images indicate segmentations of the slab anomalies along these PSBs within the upper mantle (Figures 8 and 9). Previous investigators have suggested that the slab is buckled under the two junctions and that there may be a hinge fault under the first one [*Isacks and Molnar*, 1971; *Minamino and Fujii*, 1981], and the slab is continuous to at least a few hundred kilometers depth under the second one [*Aoki*, 1974; *Utsu*, 1974; and *Hirahara*, 1981]. *P* and *S* results in this study indicate that slab is buckled under both junctions and torn apart at about 400 km depth.

Kanamori [1971] proposed a model to interpret the opposite first motions between a great Tokachi-Oki earthquake ($M_s \sim 8.0$) and its largest aftershocks ($M_s \sim 7.5$) under the first junction. The model suggests that a tear exists along the junction but the two segments are held together by lateral compression. Since the separation takes place with no detectable seismic activity, we are inclined to extend Kanamori's model in the following way. We suspect that the slab is indeed broken under the junction by a tear or a hinge fault near the surface, but the two segments are kept together in the shallow region by lateral compression from the convergent geometry of the slab there. Due to differential flattening of the slab in the deep portion of the upper mantle, the lateral compression gradually diminishes with increasing depth and the separation finally takes place aseismically.

The strong slow anomalies on the ocean side of the slab in the upper mantle, which are usually not as strong as the slow regions under back arc basins, have not been discussed previously. One interpretation of the slow anomaly is that it is actually a representative of normal mantle at that depth. This interpretation will shift the anomaly amplitudes of slab and ambient mantle as listed in Table 1 to be more negative (fast). Both the *P* and *S* results show a slow background in the upper mantle, as indicated by layered means given for each panel in Figure 8 and cross sections in Figures 10 and 11. This probably suggests that the JB model is too fast in the upper mantle. *Nataf et al.* [1984, 1986] also conclude that the shallow mantle in the vicinity of the Pacific subduction zones is slow for shear waves and the mantle below 300 km is fast. Some global studies of compressional waves [*Clayton and Comer*, 1983; *Hager and Clayton*, 1989; *Zhou and Clayton*, 1985] indicate that the JB model is, in general, too fast in the lower mantle above 900 km depth, too slow from 900 to 1100 km and then too fast again to about 1900 km. The contour pattern of the slow anomalies under the back arc basin near Honshu seems to support the wedge flow model [*McKenzie*, 1969; *Toksöz and Hsui*, 1978], the absence of intermediate and deep earthquakes, and the presence of volcanic activity from the island of Honshu to the northern Phillippine Sea.

7. CONCLUSIONS

Images of three-dimensional *P* and *S* velocity structures under the island arcs of the northwest Pacific have been well resolved by a tomographic inversion method. A grouping and sorting of rays according to source and station areas considerably reduces the noise of the data. Analysis of resolution and noise show that the images are generally resolved well. The resulting velocity models substantially reduce the variance of the data. There are strong high-velocity anomalies associated with the Wadati-Benioff zone. Although the earthquakes are generally embedded in fast regions, the dip of the Wadati-Benioff zone seismicity sometimes differs from the dip of the high-velocity regions. The *P* and *S* results correlate well in most parts of the upper mantle. Laterally, the

amplitude of the shear anomalies is around one and a half times that of the compressional anomalies in percentage. Based on our interpretation, the slab anomalies appear contorted and broadened with depth in most parts of the upper mantle, while fingering and spreading of the slab occurs in the transition zone. The slab usually flattens to subhorizontal around the 670-km discontinuity, although downward continuity of fast anomalies below this depth may occur under parts of the Mariana and Kurile arcs. The shallowly dipping slab under Japan may have slipped under the edge of the Asia continent. A three-dimensional interpretive slab model of the region has been constructed based on velocity images and seismicity. The principal compressional axes of most existing focal mechanisms in the region are in agreement with the downdip direction of the seismic slab in our images. The depth at which compression begins to dominate the downdip stress regime in the slab apparently depends on the dip and the contortion of the slab in the region. Our results support the hypothesis that the fingering and spreading of slab anomalies above or around the upper mantle-lower mantle boundary and the relationship with deep seismic activity reflects the behavior of the descending lithosphere. These features are caused by the slab encountering a barrier of some form near that boundary. We cannot resolve whether the slab sometimes penetrates the boundary or the boundary is simply depressed underneath the subduction zone. If the slab does cross the boundary, however, it appears not to retain the form of a single coherent sheet.

Acknowledgments. We thank Don L. Anderson for stimulating discussions and critical reading of the manuscript. Some useful comments by T. Tanimoto are appreciated. Several thorough, anonymous reviews improved the text. Work was supported by National Science Foundation grants EAR 83-17623. Contribution No. 4627, Division of Geological and Planetary Sciences, California Institute of Technology.

REFERENCES

Anderson, D. L., Chemical stratification of the mantle, *J. Geophys. Res.*, *84*, 6297-6298, 1979.

Anderson, D. L., Chemical inhomogeneity of mantle above 670 km transition, *Nature*, *307*, 114, 1984.

Anderson, D. L., Thermally induced phase changes, lateral heterogeneity of the mantle, continental roots and deep slab anomalies, *J. Geophys. Res.*, *92*, 13,968-13,980, 1987*a*.

Anderson, D. L., A seismic equation of state, II, Shear properties and thermodynamics of the lower mantle, *Phys. Earth Planet. Inter.*, *45*, 307-323, 1987*b*.

Anderson, D. L., and J. Bass, Transition region of the Earth's upper mantle, *Nature*, *320*, 321-328, 1986.

Ansell, J. H., and D. Gubbins, Anomalous high-frequency wave propagation from the Tonga-Kermadec seismic zone to New Zealand, *Geophys. J. R. Astron. Soc.*, *85*, 93-106, 1986.

Aoki, H., Plate tectonics of arc-junction at central Japan, *J. Phys. Earth*, *22*, 141-161, 1974.

Barazangi, M., and B. Isacks, A comparison of the spatial distribution of mantle earthquakes determined from data produced by local and by teleseismic networks for the Japan and Aleutian arcs, *Bull. Seismol. Soc. Am.*, *69*, 1763-1770, 1979.

Barley, B. J., J. A. Hudson, and A. Douglas, *S* to *P* scattering at the 650 km discontinuity, *Geophys. J. R. Astron. Soc.*, *69*, 159-172, 1982.

Bock, G., The effect of the descending lithosphere beneath the Tonga island arc on *P* wave travel-time residuals at the Warramunga Seismic Array, *Phys. Earth Planet. Inter.*, *25*, 360-371, 1981.

Bock, G., *P* wave travel times from deep and intermediate-depth earthquakes to local seismic station and the subducted slab of oceanic lithosphere beneath the Tonga island arc, *J. Geophys. Res.*, *92*, 13,863-13,877, 1987.

Bock, G., and J. Ha, Short-period *S-P* conversion in the mantle at a depth near 700 km, *Geophys. J. R. Astron. Soc.*, *77*, 593-615, 1984.

Burbach G. V., and C. Frohlich, Intermediate and deep seismicity and lateral structure of subducted lithosphere in the Circum-Pacific region, *Rev. Geophys.*, *24*, 833-874, 1986.

Chandra, U., Combination of *P* and *S* data for determination of earthquake focal mechanism, *Bull. Seismol. Soc. Am.*, *61*, 1655-1673, 1971.

Clayton, R. W., and R. P. Comer, A tomographic analysis of mantle heterogeneities from body wave travel times, *Eos Trans. AGU*, *64*, 776, 1983.

Creager, K. C., and T. H. Jordan, Slab penetration into the lower mantle, *J. Geophys. Res.*, *89*, 3031-3049, 1984.

Creager, K. C., and T. H. Jordan, Slab penetration into the lower mantle beneath the Mariana and other island arcs of the northwest Pacific, *J. Geophys. Res.*, *91*, 3573-3580, 1986.

Davies, G. F., Mechanics of subducted lithosphere, *J. Geophys. Res.*, *85*, 6304-6318, 1980.

Davies, J. H., and R. W. Clayton, Lower mantle *S*-wave tomography, *Eos Trans. AGU*, *67*, 1099, 1986.

Davies, J. H., and R. W. Clayton, Error analysis of a shear wave mantle tomographic inversion, *Eos Trans. AGU*, *68*, 1376, 1987.

Davies, J. H., O. Gudmundsson, and R. W. Clayton, Errors and small scale structure inferred from areal statistics of ISC residuals, *Seismol. Res. Lett.*, *59*, 40, 1988.

Dines, K. A., and R. J. Lytle, Computerized geophysical tomography, *Proc. IEEE*, *67*, 1065-1073, 1979.

Dziewonski, A. M., and F. Gilbert, The effects of small, aspherical perturbations on travel times and a re-examination of the corrections for ellipticity, *Geophys. J. R. Astron. Soc.*, *44*, 7-17, 1976.

Dziewonski, A. M., and J. H. Woodhouse, An experiment in the systematic study of global seismicity: Centroid moment tensor solutions for 201 moderate and large earthquakes of 1981, *J. Geophys. Res.*, *88*, 3247-3271, 1983.

Dziewonski, A. M., A. Friedman, D. Giardini, and J. H. Woodhouse, Global seismicity of 1982: Centroid-moment tensor solutions for 308 earthquakes, *Phys. Earth Planet. Inter.*, *33*, 76-90, 1983*a*.

Dziewonski, A. M., A. Friedman, and J. H. Woodhouse, Centroid-moment tensor solutions for January-March 1983, *Phys. Earth Planet. Inter.*, *33*, 71-75, 1983*b*.

Dziewonski, A. M., J. E. Franzen, and J. H. Woodhouse, Centroid-moment tensor solutions for April-June 1983, *Phys. Earth Planet. Inter.*, *33*, 243-249, 1983*c*.

Dziewonski, A. M., J. E. Franzen, and J. H. Woodhouse, Centroid-moment tensor solutions for July-September 1983, *Phys. Earth Planet. Inter.*, *34*, 1-8, 1984*a*.

Dziewonski, A. M., J. E. Franzen, and J. H. Woodhouse, Centroid-moment tensor solutions for October-December 1983, *Phys. Earth Planet. Inter.*, *34*, 129-136, 1984*b*.

Dziewonski, A. M., J. E. Franzen, and J. H. Woodhouse, Centroid-moment tensor solutions for January-March 1984, *Phys. Earth Planet. Inter.*, *34*, 209-219, 1984*c*.

Dziewonski, A. M., J. E. Franzen, and J. H. Woodhouse, Centroid-moment tensor solutions for April-June 1984, *Phys. Earth Planet. Inter.*, *37*, 87-96, 1985*a*.

Dziewonski, A. M., J. E. Franzen, and J. H. Woodhouse, Centroid-moment tensor solutions for July-September 1984, *Phys. Earth Planet. Inter.*, *38*, 203-213, 1985*b*.

Dziewonski, A. M., J. E. Franzen, and J. H. Woodhouse, Centroid-moment tensor solutions for October-December 1984, *Phys. Earth Planet. Inter.*, *39*, 147-156, 1985*c*.

Dziewonski, A. M., J. E. Franzen, and J. H. Woodhouse, Centroid-moment tensor solutions for January-March 1985, *Phys. Earth Planet. Inter.*, *40*, 249-258, 1985*d*.

Dziewonski, A. M., J. E. Franzen, and J. H. Woodhouse, Centroid-moment tensor solutions for April-June 1985, *Phys. Earth Planet. Inter.*, *41*, 215-224, 1986*a*.

Dziewonski, A. M., J. E. Franzen, and J. H. Woodhouse, Centroid-moment tensor solutions for July-September 1985, *Phys. Earth Planet. Inter.*, *42*, 205-214, 1986*b*.

Dziewonski, A. M., J. E. Franzen, and J. H. Woodhouse, Centroid-moment tensor solutions for October-December 1985, *Phys. Earth Planet. Inter.*, *43*, 185-195, 1986*c*.

Dziewonski, A. M., G. Ekström, J. E. Franzen, and J. H. Woodhouse, Global seismicity of 1977: Centroid-moment tensor solutions for 471 earthquakes, *Phys. Earth Planet. Inter.*, *45*, 11-36, 1987*a*.

Dziewonski, A. M., G. Ekström, J. E. Franzen, and J. H. Woodhouse, Global seismicity of 1978: Centroid-moment tensor solutions for 512 earthquakes, *Phys. Earth Planet. Inter.*, *46*, 316-342, 1987*b*.

Dziewonski, A. M., G. Ekström, J. E. Franzen, and J. H. Woodhouse, Global seismicity of 1979: Centroid-moment tensor solutions for 524 earthquakes, Phys. Earth Planet. Inter., 48, 18-46, 1987*c*.

Dziewonski, A. M., G. Ekström, J. E. Franzen, and J. H. Woodhouse,

Centroid-moment tensor solutions for January-March 1986, *Phys. Earth Planet. Inter.*, *45*, 1-10, 1987*d*.

Dziewonski, A. M., G. EkstrÖm, J. E. Franzen, and J. H. Woodhouse, Centroid-moment tensor solutions for April-June 1986, *Phys. Earth Planet. Inter.*, *45*, 229-239, 1987*e*.

Dziewonski, A. M., G. EkstrÖm, J. E. Franzen, and J. H. Woodhouse, Centroid-moment tensor solutions for July-September 1986, *Phys. Earth Planet. Inter.*, *46*, 305-315, 1987*f*.

Dziewonski, A. M., G. EkstrÖm, J. H. Woodhouse, and G. Zwart, Centroid-moment tensor solutions for October-December 1986, *Phys. Earth Planet. Inter.*, *48*, 5-17, 1987*g*.

Dziewonski, A. M., G. EkstrÖm, J. E. Franzen, and J. H. Woodhouse, Global seismicity of 1980: Centroid-moment tensor solutions for 515 earthquakes, *Phys. Earth Planet. Inter.*, *50*, 127-154, 1988*a*.

Dziewonski, A. M., G. EkstrÖm, J. E. Franzen, and J. H. Woodhouse, Global seismicity of 1981: Centroid-moment tensor solutions for 542 earthquakes, *Phys. Earth Planet. Inter.*, *50*, 155-182, 1988*b*.

Dziewonski, A. M., G. EkstrÖm, J. H. Woodhouse, and G. Zwart, Centroid-moment tensor solutions for January-March 1987, *Phys. Earth Planet. Inter.*, *50*, 116-126, 1988*c*.

Dziewonski, A. M., G. EkstrÖm, J. H. Woodhouse, and G. Zwart, Centroid-moment tensor solutions for April-June 1987, *Phys. Earth Planet. Inter.*, *50*, 215-225, 1988*d*.

Dziewonski, A. M., G. EkstrÖm, J. H. Woodhouse, and G. Zwart, Centroid-moment tensor solutions for July-September 1987, *Phys. Earth Planet. Inter.*, *53*, 1-11, 1988*e*.

Dziewonski, A. M., G. EkstrÖm, J. E. Franzen, and J. H. Woodhouse, Global seismicity of 1982 and 1983: Centroid-moment tensor solutions for 553 earthquakes, *Phys. Earth Planet. Inter.*, *53*, 17-45, 1988*f*.

Engdahl, E. R., and E. A. Flinn, Seismic waves reflected from discontinuities within the Earth's upper mantle, *Science*, *163*, 177-179, 1969.

Engdahl, E. R., and D. Gubbins, Simultaneous travel-time inversion for earthquake location and subduction zone structure in the central Aleutian Islands, *J. Geophys. Res.*, *92*, 13,855-13,862, 1987.

Faber, S., and G. Müller, Converted phases from the mantle transition zone observed at European stations, *J. Geophys.*, *54*, 183-194, 1984.

Fischer, K., T. H. Jordan, and K. C. Creager, Seismic constraints on the morphology of deep slabs, *J. Geophys. Res.*, *93*, 4773-4783, 1988.

Fitch, T. J., In situ *P* wave velocities in deep earthquake zones of the SW Pacific: Evidence for a phase boundary between the upper and lower mantle, in *Island Arcs, Deep Sea Trenches and Back-Arc Basins*, Maurice Ewing Ser. vol. 1, edited by M. Talwani and W. C. Pitman III, pp.99-114, AGU, Washington, D. C., 1977.

Frohlich, C., and M. Barazangi, A regional study of mantle velocity variations beneath eastern Australia and the southwestern Pacific using short-period recording of *P*, *S*, *PcP*, *ScP* and *ScS* waves produced by Tongan deep earthquakes, *Phys. Earth Planet. Inter.*, *21*, 1-14, 1980.

Fujita, K., and H. Kanamori, Double seismic zone and stresses of intermediate depth earthquakes, *Geophys. J. R. Astron. Soc.*, *66*, 131-156, 1981.

Giardini, D., Systematic analysis of deep seismicity: 200 centroid-moment tensor solutions for earthquakes between 1977 and 1980, *Geophys. J. R. Astron. Soc.*, *77*, 883-914, 1984.

Giardini, D., and J. H. Woodhouse, Deep seismicity and modes of deformation in Tonga subduction zone, *Nature*, *307*, 505-509, 1984.

Giardini, D., and J. H. Woodhouse, Horizontal shear flow in the mantle beneath the Tonga arc, *Nature*, *319*, 551-555, 1986.

Gilbert, P., Iterative methods for the reconstruction of three-dimensional objects from projections, *J. Theor. Biol.*, *36*, 105-117, 1972.

Grand, S. P., Tomographic inversion for shear velocity beneath the North American plate, *J. Geophys. Res.*, *92*, 14,065-14,090, 1987.

Gurnis, M., and B. H. Hager, Controls on the structure of subducted slabs and the viscosity of the lower mantle, *Nature*, *335*, 317-321, 1988.

Gutenberg, B., and Richter, C. F., *Seismicity of the Earth*, 2nd ed., Princeton University Press, Princeton, N.J., 1954.

Hager, B. H., Subducted slabs and the geoid: constraints on mantle rheology and flow, *J. Geophys. Res.*, *89*, 6003-6015, 1984.

Hager, B. H., and R. W. Clayton, Constraints on the structure of mantle convection using seismic observations, flow models, and the geoid, in *Mantle Convection*, edited by W. R. Peltier, pp.657-763, Gordon and Breach, New York, 1989.

Hager, B. H., and R. J. O'Connell, A simple global model of plate dynamics and mantle convection, *J. Geophys. Res.*, *86*, 4843-4867, 1981.

Hager, B. H., and A. Raefsky, Deformation of seismic discontinuities and the scale of mantle convection, *Eos Trans. AGU*, *62*, 1074, 1981.

Hager, B. H., R. W. Clayton, M. A. Richards, R. P. Comer, and A. M. Dziewonski, Lower mantle heterogeneity, dynamic topography and the geoid, *Nature*, *313*, 541-545, 1985.

Hirahara, K., A large-scale three-dimensional seismic structure under the Japan islands and the Sea of Japan, *J. Phys. Earth*, *25*, 393-417, 1977.

Hirahara, K., Three-dimensional seismic structure beneath southwest Japan: The subducting Philippine Sea plate, *Tectonophysics*, *79*, 1-41, 1981.

Hirahara, K., and T. Mikumo, Three-dimensional seismic structure of subducting lithospheric plates under the Japan islands, *Phys. Earth Planet. Inter.*, *21*, 109-119, 1980.

Hirasawa, T., A least squares method for the focal mechanism determinations from *S* wave data (2), *Bull. Earthquake Res. Inst. Univ. Tokyo*, *44*, 919-938, 1966.

Honda, H., On the mechanism of deep earthquakes and the stress in the deep layer of the Earth's crust, *Geophys. Mag. Tokyo*, *8*, 179-185, 1934.

Humphreys, E., and R. W. Clayton, Adaptation of back projection tomography to seismic travel time problems, *J. Geophys. Res.*, *93*, 1073-1085, 1988.

Humphreys, E., R. W. Clayton, and B. H. Hager, A tomographic image of mantle structure beneath southern California, *Geophys. Res. Lett.*, *11*, 625-627, 1984.

Husebye, E. S., R. A. Haddon, and D. W. King, Precursors to *P'P'* and upper mantle discontinuities, *J. Geophys.*, *43*, 535-543, 1977.

Ichikawa, M., Mechanism of earthquakes in and near Japan, 1950-1962, *Pap. Meteorol. Geophys. Tokyo*, *16*, 201-229, 1966.

Isacks, B. L., and M. Barazangi, Geometry of Benioff zones, lateral segmentation and downwards bending of the subducted lithosphere, in *Island Arcs, Deep Sea Trenches and Back-Arc Basins*, Maurice Ewing Ser., vol. 1, edited by M. Talwani and W. C. Pitman III, pp.99-114, AGU, Washington, D. C., 1977.

Isacks, B., and P. Molnar, Mantle earthquake mechanisms and sinking of the lithosphere, *Nature*, *223*, 1121-1124, 1969.

Isacks, B., and P. Molnar, Distribution of stresses in the descending lithosphere from a global survey of focal mechanism solution of mantle earthquakes, *Rev. Geophys.*, *9*, 103-174, 1971.

Isacks, B., J. Oliver, and L. R. Sykes, Seismology and the new global tectonics, *J. Geophys. Res.*, *73*, 5855-5899, 1968.

Jeanloz, R., and A. B. Thompson, Phase transitions and mantle discontinuities, *Rev. Geophys.*, *21*, 51-74, 1983.

Jordan, T. H., Lithospheric slab penetration into the lower mantle beneath the Sea of Okhotsk, *J. Geophys.*, *43*, 473-496, 1977.

Kamiya, S., T. Miyatake, and K. Hirahara, How deep can we see the high velocity anomalies beneath the Japan Island? *Geophys. Res. Lett.*, *15*, 828-831, 1988.

Kanamori, H., Focal mechanism of the Tokachi-Oki earthquake of May 16, 1968: Contortion of the lithosphere at the junction of two trenches, *Tectonophysics*, *12*, 1-13, 1971.

Katsumata, M., and L. R. Sykes, Seismicity and tectonics of the western Pacific: Izu-Mariana-Caroline and Ryukyu-Taiwan regions, *J. Geophys. Res.*, *74*, 5923-5948, 1969.

Kincaid, C., and P. Olson, An experimental study of subduction and slab migration, *J. Geophys. Res.*, *92*, 13,832-13,840, 1987.

Knittle, E., R. Jeanloz, and G. L. Smith, Thermal expansion of silicate perovskite and stratification of the Earth's mantle, *Nature*, *319*, 214-216, 1986.

Lay, T., and H. Kanamori, An asperity model of large earthquake sequences, in *Earthquake Prediction*, edited by D. W. Simpson and P. G. Richards, pp.579-592, AGU, Washington, D. C., 1981.

McKenzie, D. P., Speculations on the consequences and causes of plate motions, *Geophys. J. R. Astron. Soc.*, *18*, 1-32, 1969.

Minamino, T., and N. Fujii, The effect of the contorted "nose" of a subducting slab on the stress field in the continental lithosphere at an arc-arc junction, *Geophys. J. R. Astron. Soc.*, *67*, 145-158, 1981.

Nakanishi, I., Reflections of *P'P'* from upper mantle discontinuities beneath the Mid-Atlantic Ridge, *Geophys. J.*, *93*, 335-346, 1988.

Nataf, H.-C., I. Nakanishi, and D. L. Anderson, Anisotropy and shear-velocity heterogeneities in the upper mantle, *Geophys. Res. Lett.*, *11*, 109-112, 1984.

Nataf, H.-C., I. Nakanishi, and D. L. Anderson, Measurements of mantle wave velocities and inversion for lateral heterogeneities and anisotropy, 3, Inversion, *J. Geophys. Res.*, *91*, 7261-7307, 1986.

Nieman, T. L., K. A. Wagner, and K. Fujita, Effects of subducting slabs

on teleseismic hypocentral determinations--Theoretical Calculations, *Eos Trans. AGU, 65*, 234, 1984.

Nolet, G., Solving or resolving inadequate and noisy tomographic systems *J. Comput. Phys., 61*, 463-482, 1985.

Oike, K., On the nature of the occurrence of intermediate and deep earthquakes, 1, The world wide distribution of the earthquake generating stress, *Bull. Disaster. Prev. Res. Inst. Kyoto Univ., 20*, 145-182, 1971.

Olson, A. H., A Chebyshev condition for accelerating convergence of iterative tomographic methods--solving large least squares problems, *Phys. Earth Planet. Inter., 47*, 333-345, 1987.

Richards, P. G., Seismic waves reflected from velocity gradient anomalies within the Earth's upper mantle, *J. Geophys., 38*, 517-527, 1972.

Richter, F. M., Focal mechanisms and seismic energy release of deep and intermediate earthquakes in the Tonga-Kermadec region and their bearing on the depth extent of mantle flow, *J. Geophys. Res., 84*, 6783-6795, 1979.

Ringwood, A. E., and T. Irifune, Layered convection in a grossly homogeneous mantle, *Eos Trans. AGU, 69*, 486, 1988.

Ritsema, A. R., The mechanism of some deep and intermediate earthquakes in the region of Japan, *Bull. Earthquake Res. Inst. Univ. Tokyo, 43*, 39-52, 1965.

Roecker, S. W., Velocity structure in the Izu-Bonin seismic zone and the depth of the olivine-spinel phase transition in the slab, *J. Geophys. Res., 90*, 7771-7794, 1985.

Sengupta, M. K., and M. N. Toksöz, The amplitudes of *P* waves and magnitude corrections for deep focus earthquakes, *J. Geophys. Res., 82*, 2971-2980, 1977.

Silver, P. G., and W. W. Chan, Observations of body wave multipathing from broadband seismograms: Evidence for lower mantle slab penetration beneath the Sea of Okhotsk, *J. Geophys. Res., 91*, 13,787-13,802, 1986.

Sondergeld, C. H., B. L. Isacks, M. Barazangi, and S. Billinton, A search for velocity anomalies near the deep portions of the inclined seismic zone of Tonga island arc, *Bull. Seismol. Soc. Am., 67*, 537-541, 1977.

Spencer, C. P., and E. R. Engdahl, A joint hypocenter location and velocity inversion technique applied to the central Aleutians, *Geophys. J. R. Astron. Soc., 72*, 399-415, 1983.

Spencer, C. P., and D. Gubbins, Travel-time inversion for simultaneous earthquake location and velocity structure determination in laterally varying media, *Geophys. J. R. Astron. Soc., 63*, 95-116, 1980.

Stark, P. B., and C. Frohlich, The depths of the deepest deep earthquakes, *J. Geophys. Res., 90*, 1859-1869, 1985.

Stauder, W., and L. Maulchin, Fault motion in the larger earthquakes of the Kurile-Kamchatka arc and the Kurile-Hokkaido corner, *J. Geophys. Res., 81*, 2297-2308, 1976.

Toksöz, M. N., and A. T. Hsui, Numerical studies of back-arc convection and the formation of marginal basins, *Tectonophysics, 50*, 177-196, 1978.

Toksöz, N., J. W. Minear, and B. R. Julian, Temperature field and geophysical effects of a down-going slab, *J. Geophys. Res., 76*, 1113-1138, 1971.

Utsu, T., Seismological evidence for anomalous structure of island arcs with special reference to the Japanese region, *Rev. Geophys., 9*, 839-890, 1971.

Utsu, T., Space-time pattern of large earthquakes occurring off the Pacific coast of the Japanese islands, *J. Phys. Earth, 22*, 325-342, 1974.

Vassiliou, M. S., and B. H. Hager, Subduction zone earthquakes and stress in slabs, *Pure Appl. Geophys., 128*, 547-624, 1988.

Vidale, J. E., Waveform effects of a high-velocity subducted slab, *Geophys. Res. Lett., 14*, 542-545, 1987.

Wadati, K., On the activity of deep-focus earthquakes in the Japan Island and neighbourhood, *Geophys. Mag. Tokyo, 8*, 305-326, 1935.

Wallace, T. C., and W. E. Holt, The 670 km discontinuity and precursors to *P'P'*: Implications for the sharpness of the boundary and its global extent, *Eos Trans. AGU, 69*, 1333, 1988.

Whitcomb, J. H., and D. L. Anderson, Reflections of *PP* seismic waves from discontinuities in the mantle, *J. Geophys. Res., 75*, 5713-5728, 1970.

Zhou, H., How well can we resolve the deep seismic slab with seismic tomography?, *Geophys. Res. Lett., 15*, 1425-1428, 1988.

Zhou, H., and R. W. Clayton, Mantle velocities from *PP*-waves, *Eos Trans. AGU, 66*, 975, 1985.

Zhou, H., and R. W. Clayton, Travel-time inversions for *P* and *S* velocities beneath the northwest edge of the Pacific: Slab fingering?, *Eos Trans. AGU, 68*, 1379, 1987.

Zhou, H., and R. W. Clayton, *P* wave velocities around subduction zones in the southwest Pacific, *Eos Trans. AGU, 69*, 398, 1988.

Zhou, H., D. L. Anderson, and R. W. Clayton, Modeling of residual spheres for subduction zone earthquakes, 1, Apparent slab penetration signatures in the NW Pacific caused by deep diffuse mantle anomalies, *J. Geophys. Res.*, in press, 1990.

R. W. Clayton, Seismological Laboratory 252-21, California Institute of Technology, Pasadena, CA 91125.

H. Zhou, Department of Geosciences, University of Houston, Houston, TX 77204-5503.

(Received September 26, 1988;
revised November 10, 1989;
accepted October 5, 1989.)